



Doctoral Dissertation Defense

Development of a Large-Scale Vision-Based Tactile Sensing System for Robotic Links

Ph.D. Student: Lac Van Duong

ID: s1820421

Supervisor: Associate Prof. Van Anh Ho

Second Supervisor: Prof. Hiroshi Mizuta

Dissertation Committee

- Associate Prof. Van Anh Ho, JAIST
- Prof. Hiroshi Mizuta, JAIST
- Prof. Hideyuki Murata, JAIST
- Associate Prof. JI Yonghoon, JAIST
- Prof. Kazuhiro Shimonomura, Ritsumeikan University

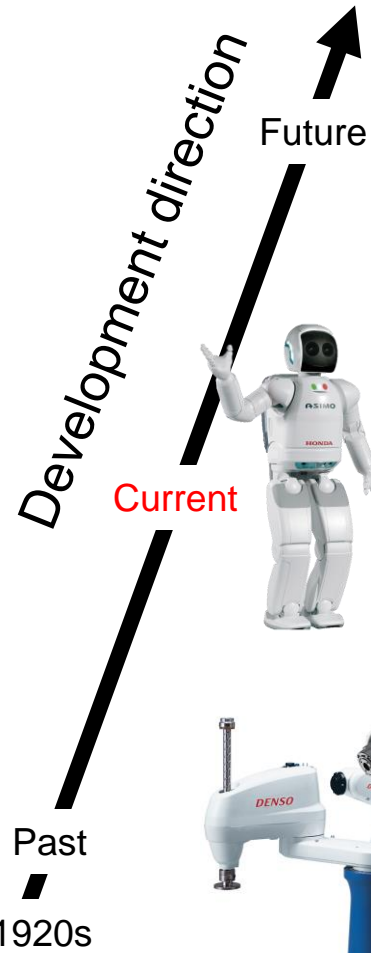
Outline

- I. Introduction
- II. Research Contents
- III. Discussion
- IV. Conclusion
- V. Future Work
- Publication
- Reference
- Acknowledgment

I. Introduction

- 1.1. Research Approach
- 1.2. Review: Tactile Sensor
- 1.4. Review: Large-Scale Robotic Tactile Skin
- 1.5. Review: Vision-Based Tactile Sensor

1.1. Research Approach



Fully actuated and sensory artificial prostheses for humans

- ✓ Enabling naturally perceive and interact with the environment

Humanoid, service and healthcare robots

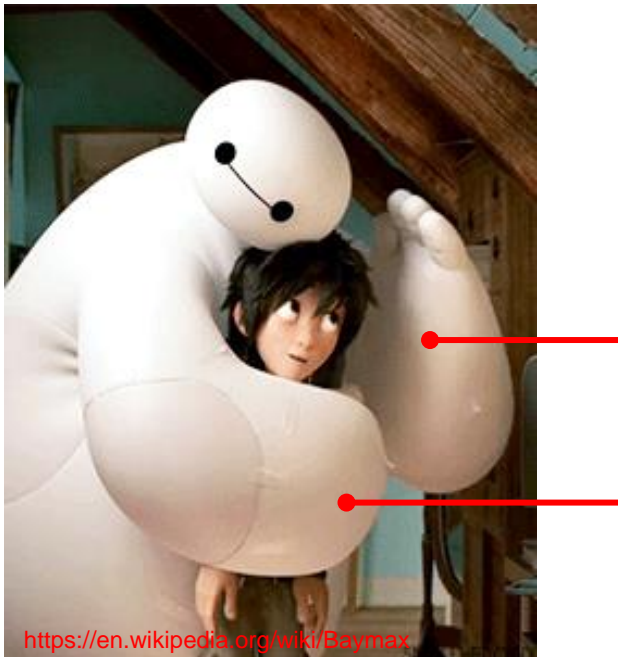
- ✓ Using many sensors: vision, microphone, force sensor.
- ✗ Lack of a whole-body tactile skin → remaining unsafe, lack of smart interaction and manipulation through touch sensing.

Traditionally Industrial robots

- ✓ High speed and accuracy
- ✗ Rigid arm and lack of sensory feedback → unsafe
- ✗ Suitable for industrial environment

1.1. Research Approach

The research desires to develop the new generation of smart robots with whole-body tactile skin.

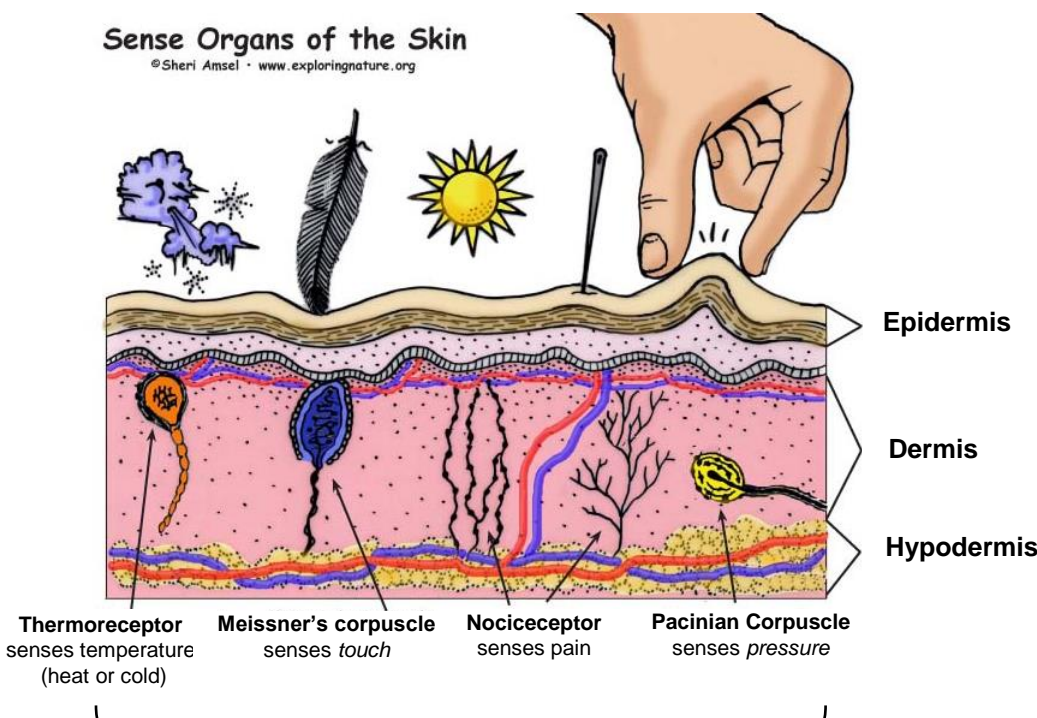


Baymax
(Fictional superhero)

- ✓. Continuous, soft, and comfortable tactile skin
- ✓. Safe and intelligent interaction

1.1. Review: Tactile Sensor

A tactile sensor is a device to detect or measure external stimuli arising from physical interaction with the environment.



<https://www.exploringnature.org/>



SynTouch BioTac [2]

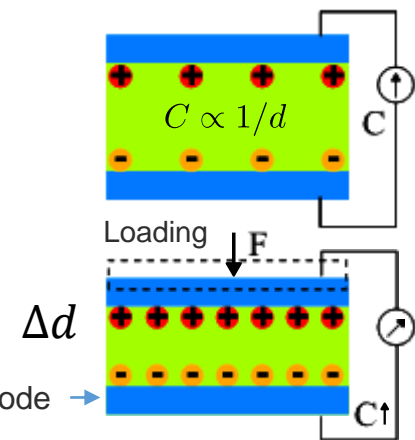
What does it sense ?

- Temperature → Thermal Camera
- Object properties (size, shape, roughness, etc.) → Vision System
- Contact pressure/force

1.1. Review: Tactile Sensor

Based on capacitive, piezoresistive, or piezoelectric transductions, etc. tactile sensors convert physical stimulus (e.g. pressure/force/strain...) into a measurable electrical signal, such as capacitance, resistance, voltage, etc.

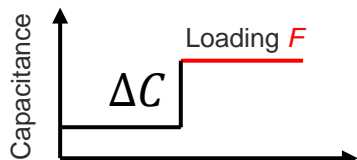
Capacitance



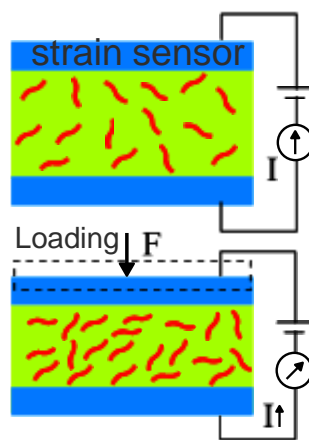
Δd

Change in capacitance

$$\rightarrow \frac{\Delta C}{C^2} \propto -\Delta d \propto F$$



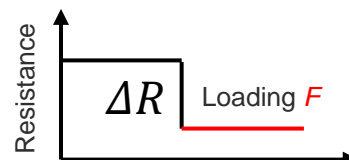
Piezoresistivity



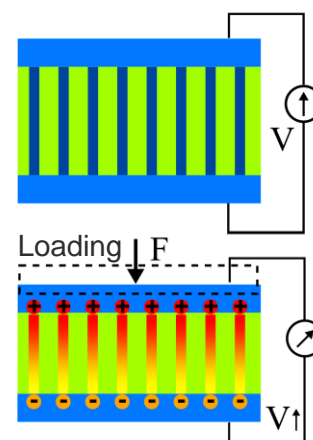
Change in resistance

$$\frac{\Delta R}{R} = (1 + 2\nu) \epsilon \propto -F$$

Poisson's ratio



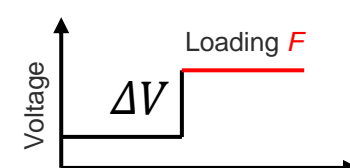
Piezoelectricity



Charge density

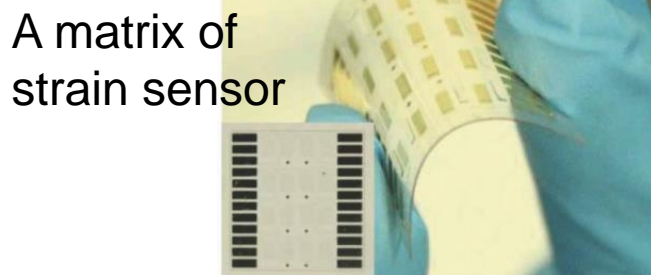
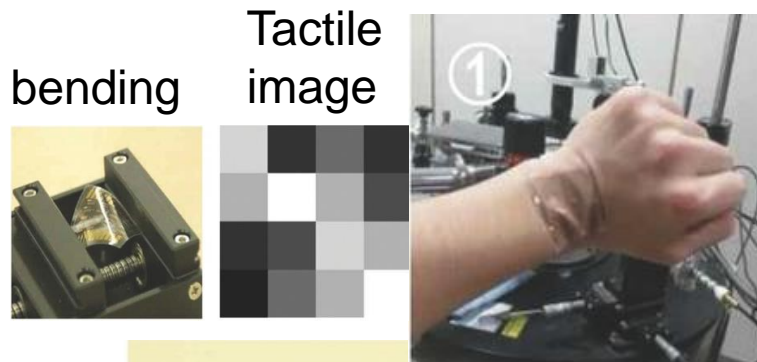
$$D_i = d_{ijk} \chi_{jk} \propto F$$

stress
piezoresistive coefficients

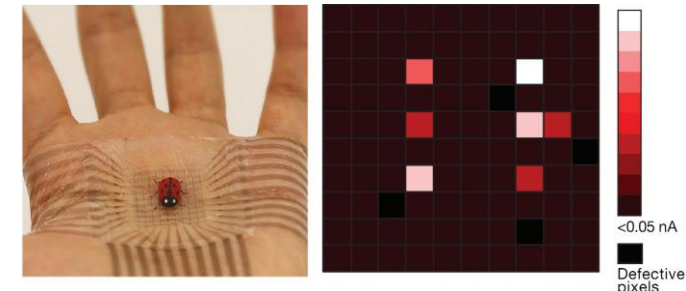


1.1. Review: Tactile Sensor

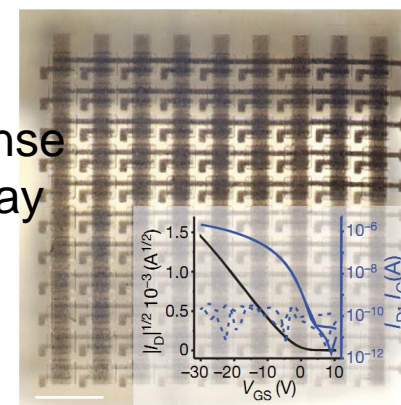
A tactile skin is normally **an array of sensing elements** with a highly **flexible/soft** structure to be wearable/comfortable on a curve 3-D surface of the robot body.



Sun et al. 2015 [3]



A circuit of dense transistors array



Wang et al. 2018 [4]

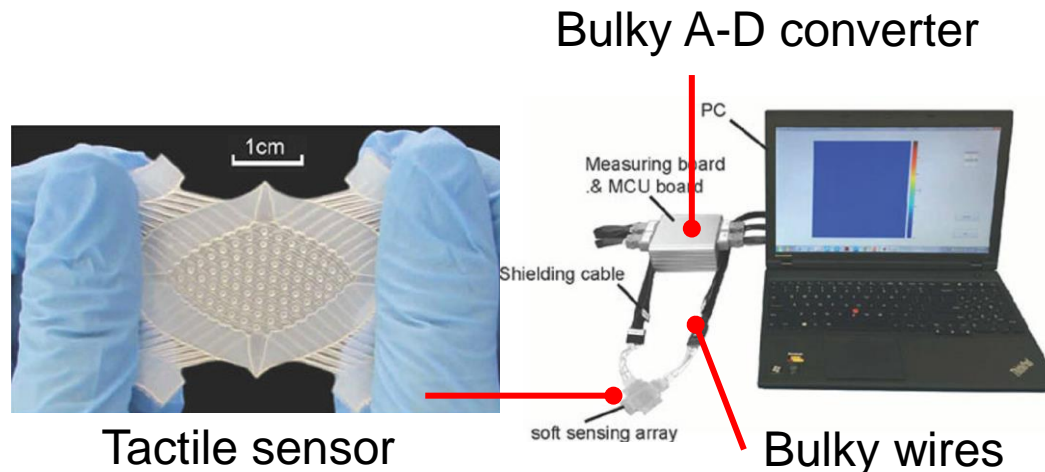
Limitation:

X. These researchers focus mainly on the development of the structure and principle without considering the **system-design level** of the large-scale sensing system

1.3. Review: Tactile Sensor

Because the challenges of the tactile sensing technology are mainly at the system-design level for the **large-scale sensing system**, i.e.,

- Bulk of wires and analog-to-digital (A-D) converters
- The complex in data acquisition and transmitting
- Risk of damage, etc.

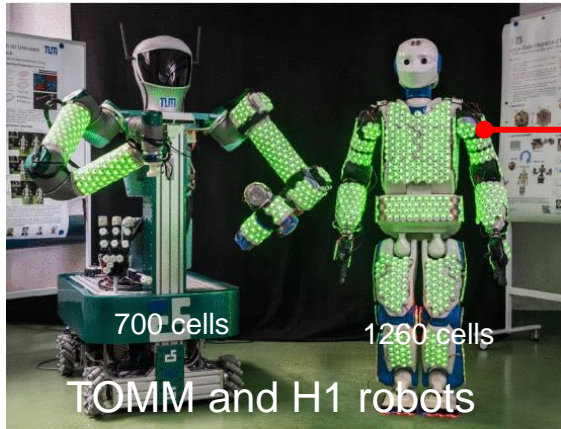


Li et al. 2017 [5]

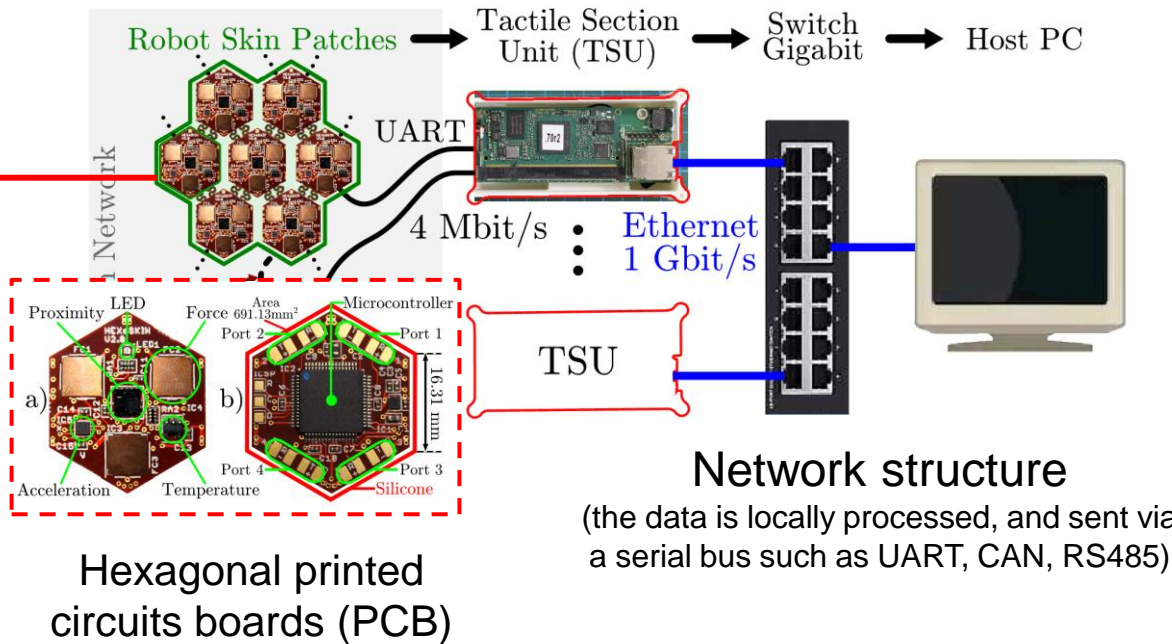
<https://ieeexplore.ieee.org/document/7947108>

1.2. Review: Large-Scale Robotic Tactile Skin

At present, the effective designs for the large-scale robot skin are the integrated electronic circuit formed by many spatially distributed modular sensing points.



Cheng et al. 2019 [7]



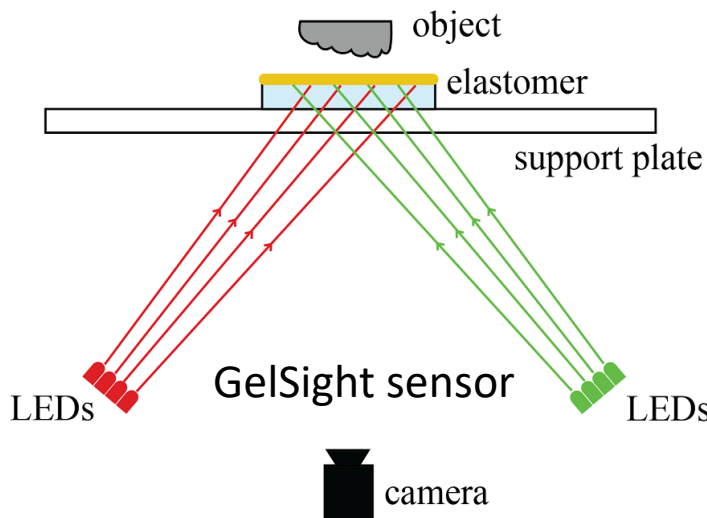
Limitations:

- X. Lack of mechanical flexibility (rigid PCB and electronic components)
- X. Low spatial resolution
- X. Complex in data networking and real-time transmitting
- X. Very expensive (e.g., 1000 cells x 100\$ = 100,000\$ ~1000 man)

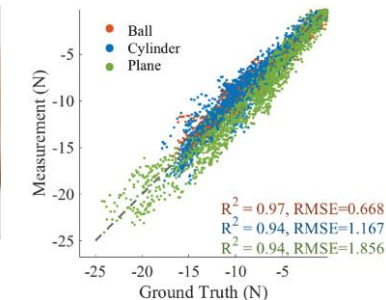
1.3. Review: Vision-Based Tactile Sensor

Vision-based tactile sensors (consisting of a camera, elastic surface, and light source) offer many advantages:

- ✓. High spatial resolution (pixel size in order of μm)
- ✓. Without the need to embed any sensing elements



Yuan et al. 2017 [8]

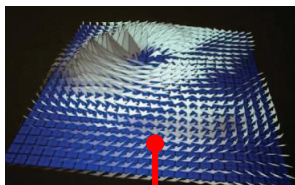
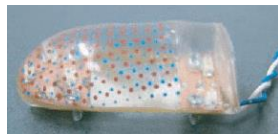


detailed surface texture

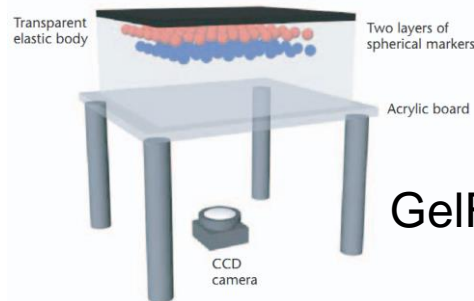
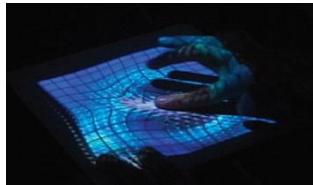
Limitations:

- X. Every sensor needs to recalibrate (a lookup table) by an experimental method
- X. The total force applied can be predicted by the machine learning method but the distribution of applied force could not be provided
- X. Only suitable for small scale (e.g., fingertip)

1.3. Review: Vision-Based Tactile Sensor

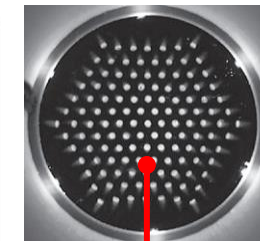
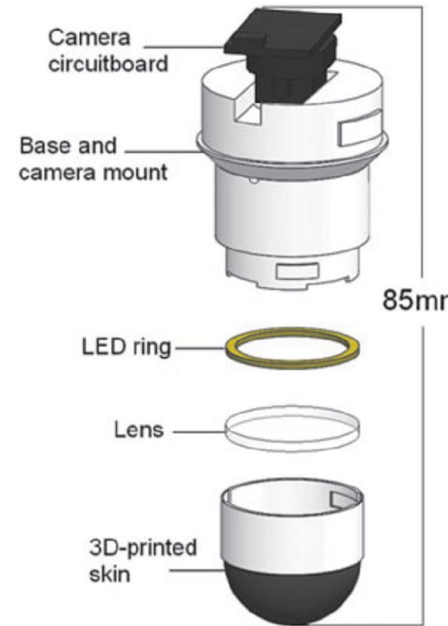


Vector distribution



GelForce sensor

Sato et al. 2009 [9]



Tactile image for machine learning

TacTip sensor

Ward-Cherrier et al. 2018 [10]

Limitations:

- X. Most of the vision-tactile sensors are small-scale (designed for the fingertip)
- X. The distribution of contact force could not be provided reasonably

Needs:

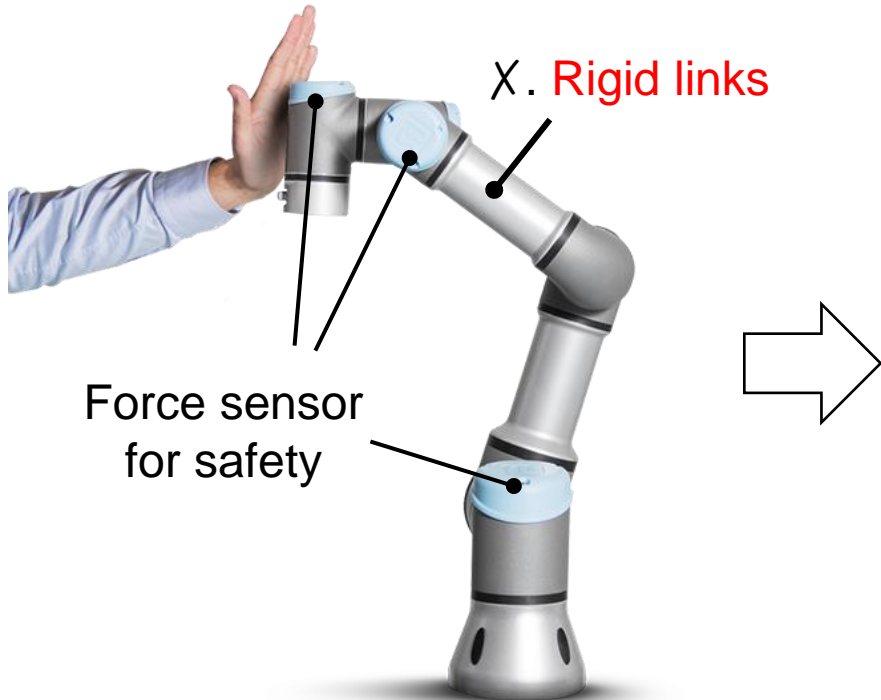
- ✓. A scalable vision-tactile sensor design for large-scale systems
- ✓. A robust technique for sensing both contact geometry and contact force.

II. Research Contents

- 2.1. Research Objective
- 2.2. System Design
- 2.3. Artificial Skin Fabrication
- 2.4. Vision-Based Model
- 2.5. Finite Element Model
- 2.6. Tactile Force Reconstruction

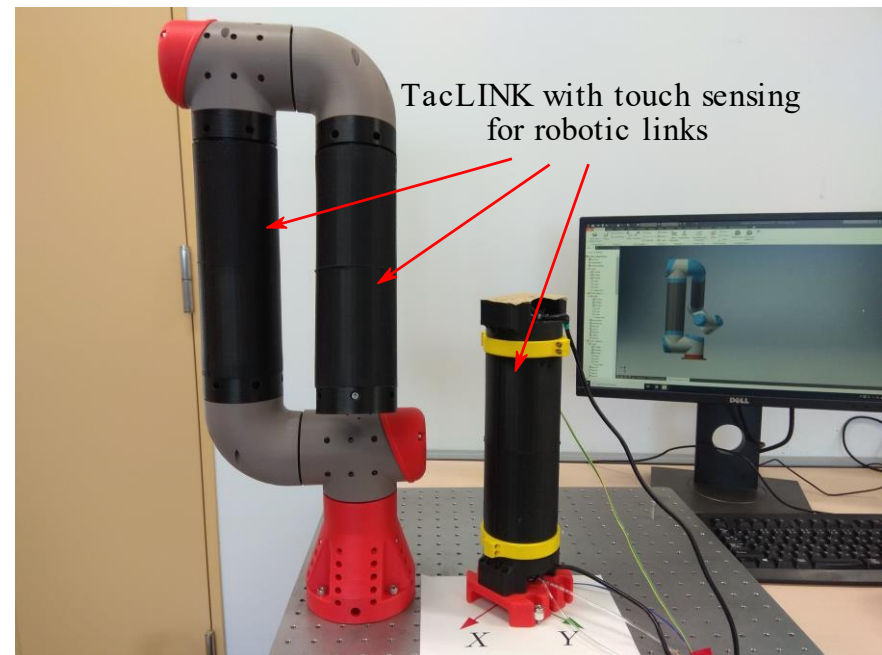
2.1. Research Objective

The research proposes a novel tactile system for robot links that are the main manipulation parts of a robot. The proposed system could be utilized widely for robotic arms, service robots, prosthetics, etc.



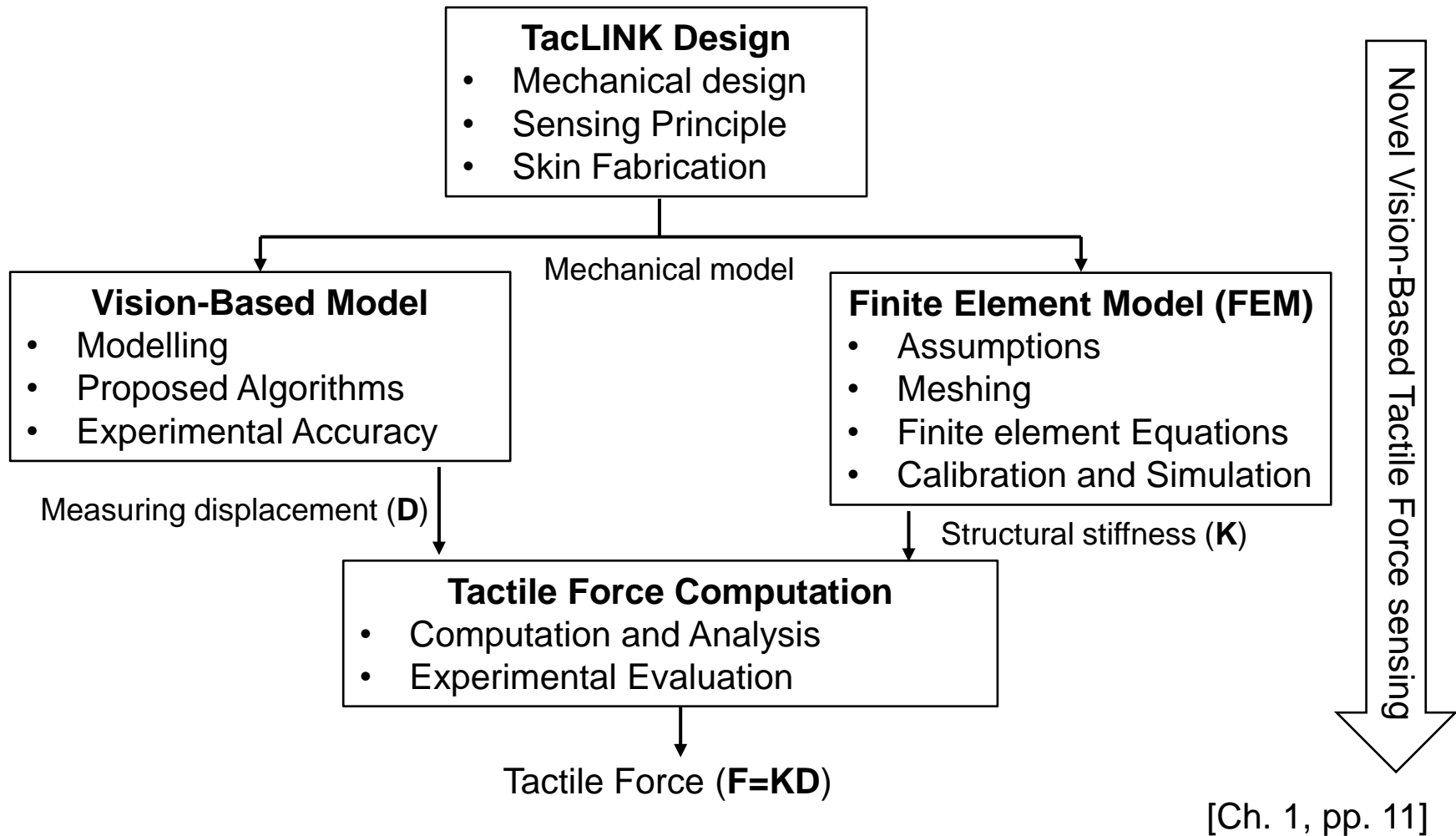
A collaborative UR3 robot

<https://www.universal-robots.com/>



The proposed tactile sensing system
for robot links (i.e., TacLINK)

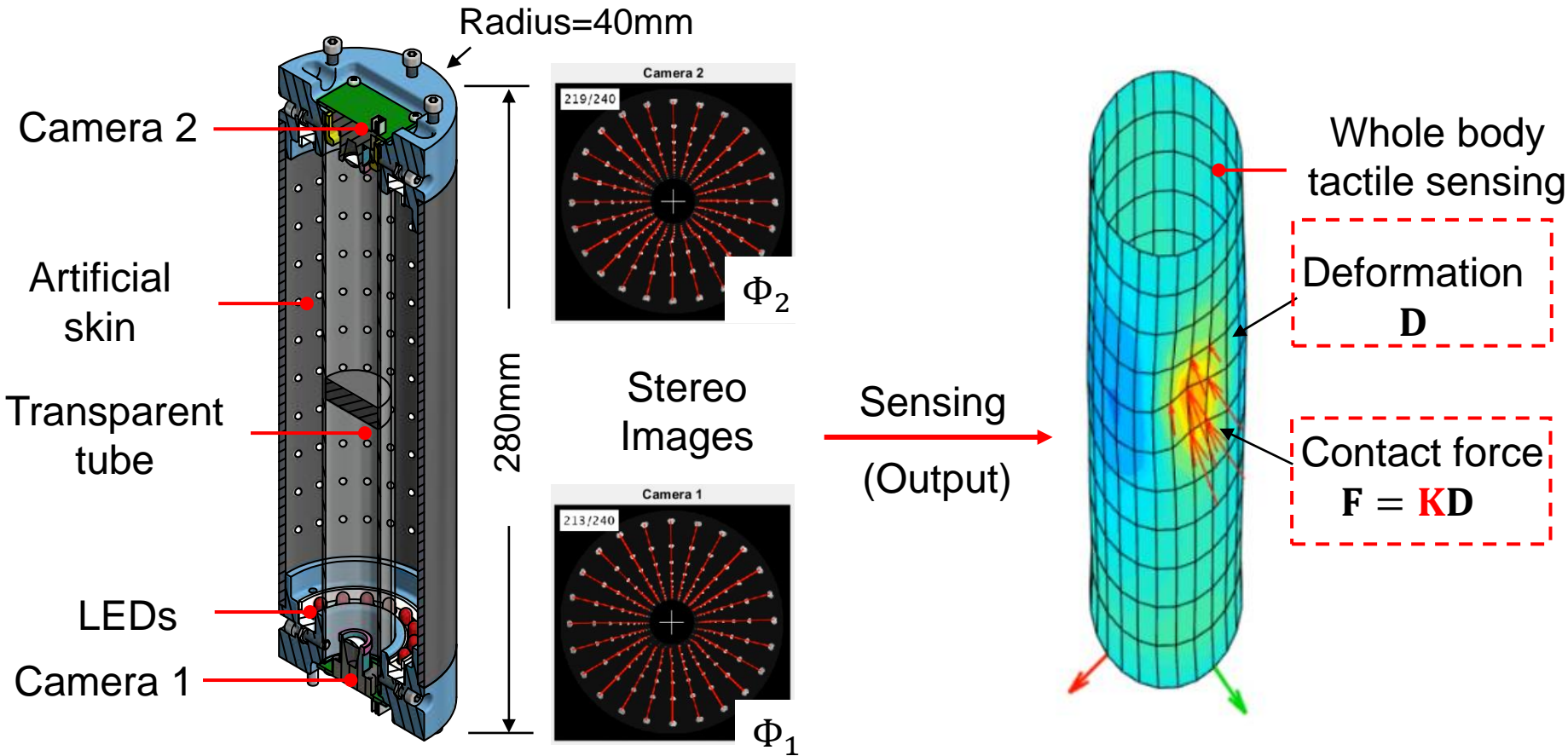
2.2. System Design



[Ch. 1, pp. 11]

The contribution of the research is the development of a novel tactile force sensing system (including design, fabrication, system modelling, proposed algorithms, FEM-based force sensing method, experimental evaluations)

2.2. System Design

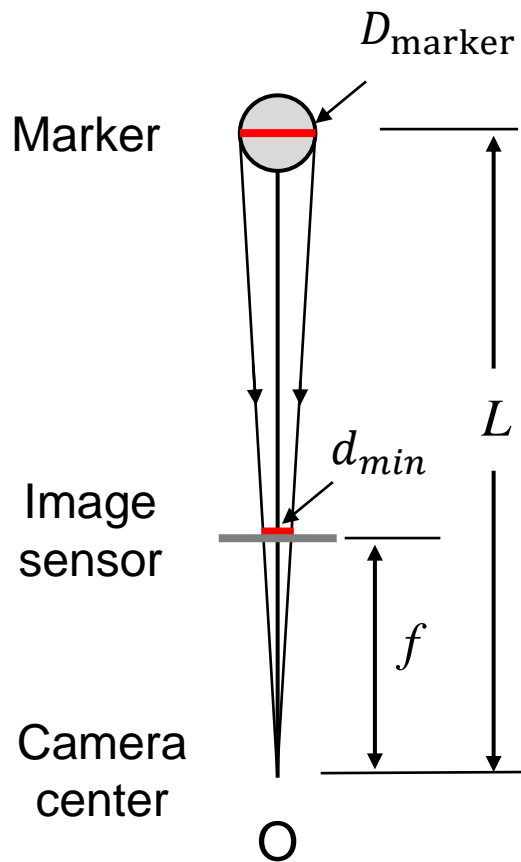


Choices: Half-section view

[Ch. 3, pp. 23-24]

- The vision system is to measure the displacement of FE nodes (FEM model) → necessity of fabricating marker points coinciding with FE nodes.
- Noted the RGB-Depth camera is only effective with facing surface → Two cameras are installed on two sides to ensure capturing entire marker points.

2.2. System Design



The projective equation of a marker:

$$\frac{d_{min}}{D_{marker}} = \frac{f}{L}$$

The length of TacLINK is limited by the detectability of the camera to the marker points. If D_{marker} is the diameter of a marker, the size of a marker on the image is

$$d = D_{marker} \frac{f}{L} > d_{min}$$

Thus, the maximum sensing length of TacLINK is

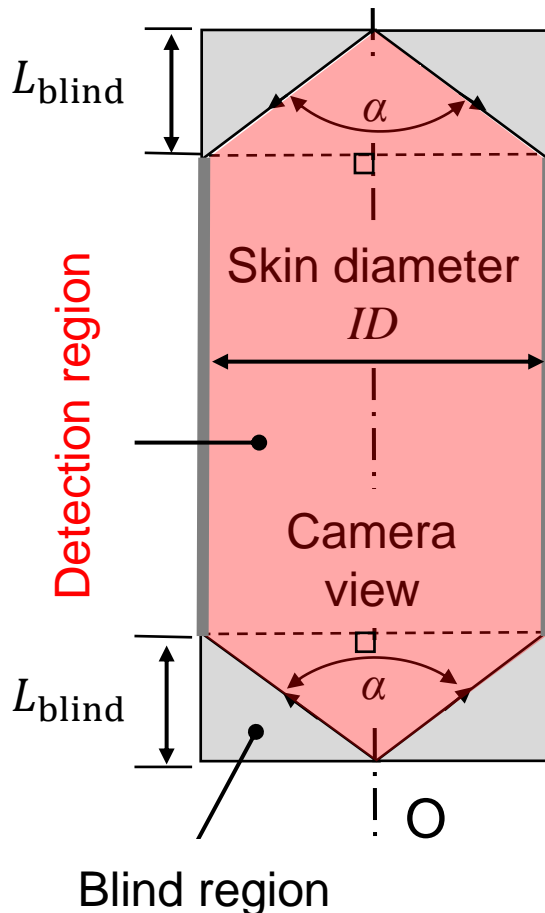
$$L < f \frac{D_{marker}}{d_{min}} = 226.5 \frac{2.8}{3} = 211(\text{mm})$$

→ Choose: $L = 198\text{mm}$

where f is the focal length of a camera in pixels, d_{min} is the minimum detectable pixel size of a marker on the image, L is the sensing length of the skin.

[Ch. 3, pp. 25]

2.2. System Design



Increasing the diameter ID of TacLINK results in increasing the blind region of TacLINK on the total length of TacLINK:

$$L_{blind} = \frac{ID}{2} \cot\left(\frac{\alpha}{2}\right)$$

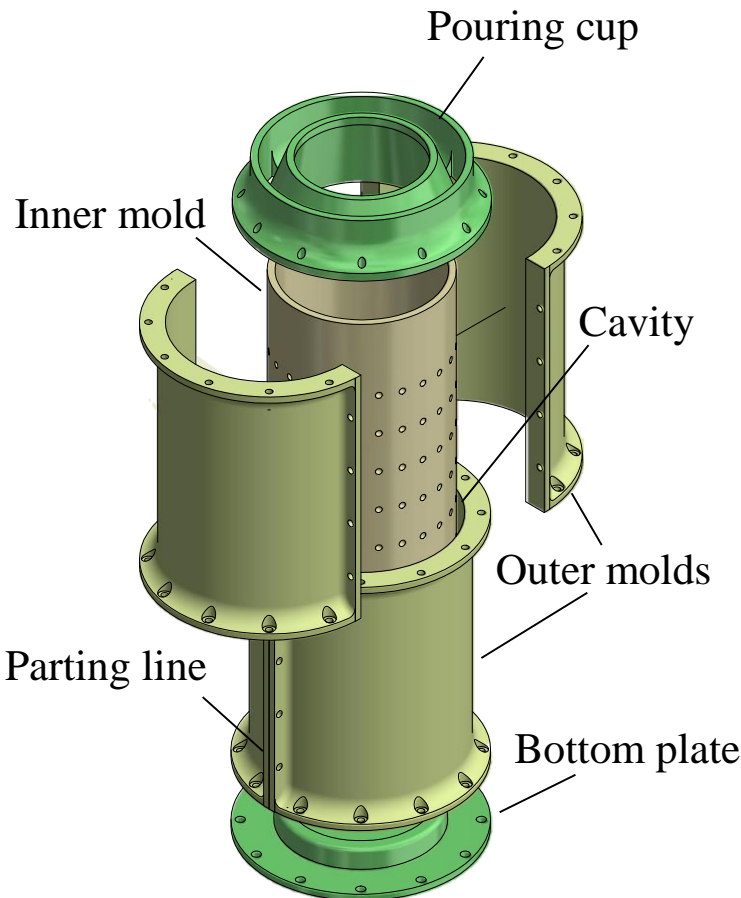
where α is the view angle of the camera.

Here, the diameter $ID = 73\text{mm}$ was chosen based on the size of the UR5 robot, so that:

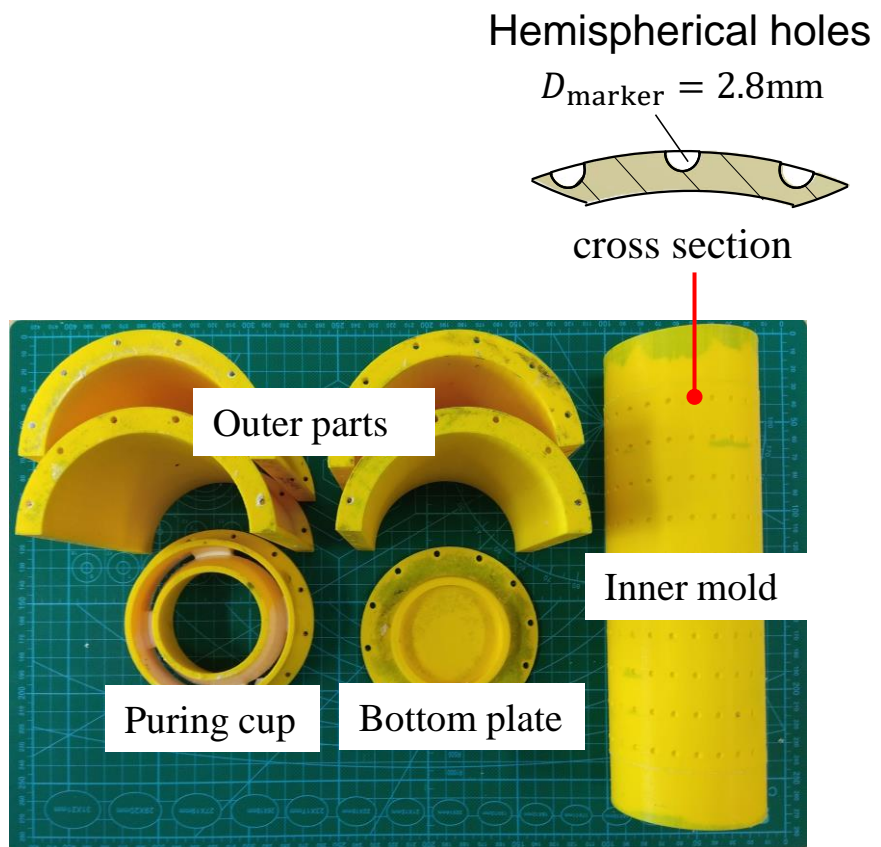
$$L_{blind} = \frac{73}{2} \cot\left(\frac{150^\circ}{2}\right) = 9.7\text{mm}$$

[Ch. 3, pp. 25-26]

2.3. Artificial Skin Fabrication

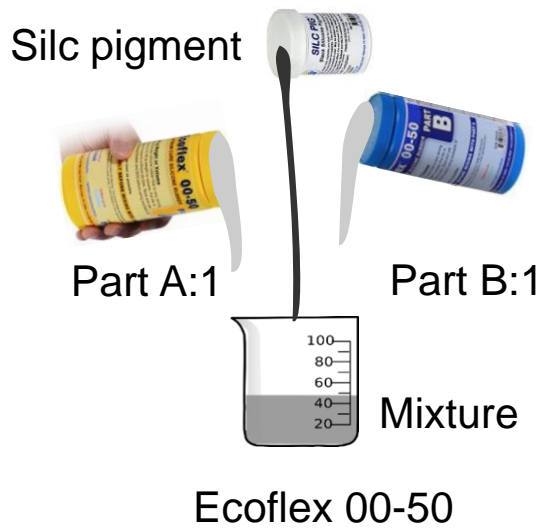


The casting mold for the skin
(designed on Autodesk Inventor 2020,
with free educational license)

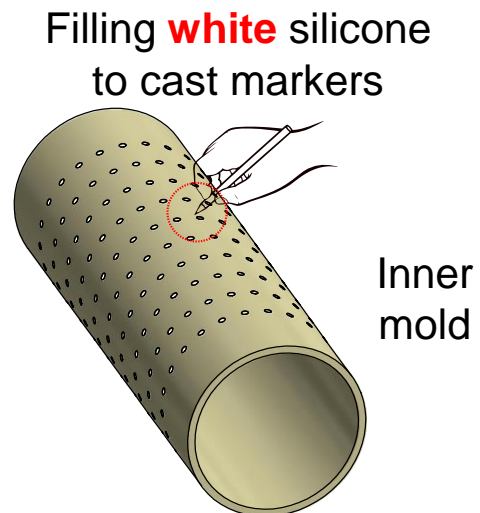


The 3-D printing parts
(printed by a 3-D printer)

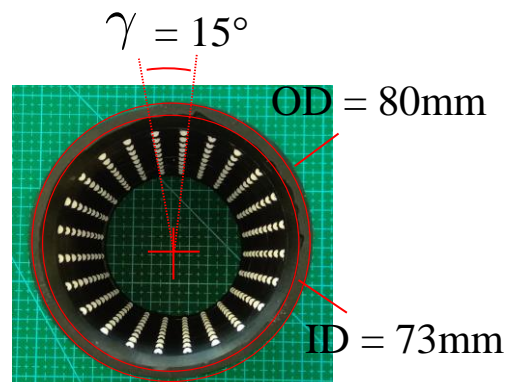
2.3. Artificial Skin Fabrication



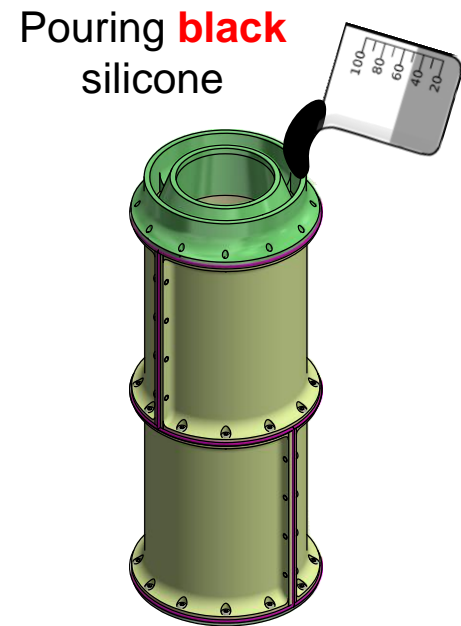
Step 1: Mixing silicone



Step 2: Casing markers



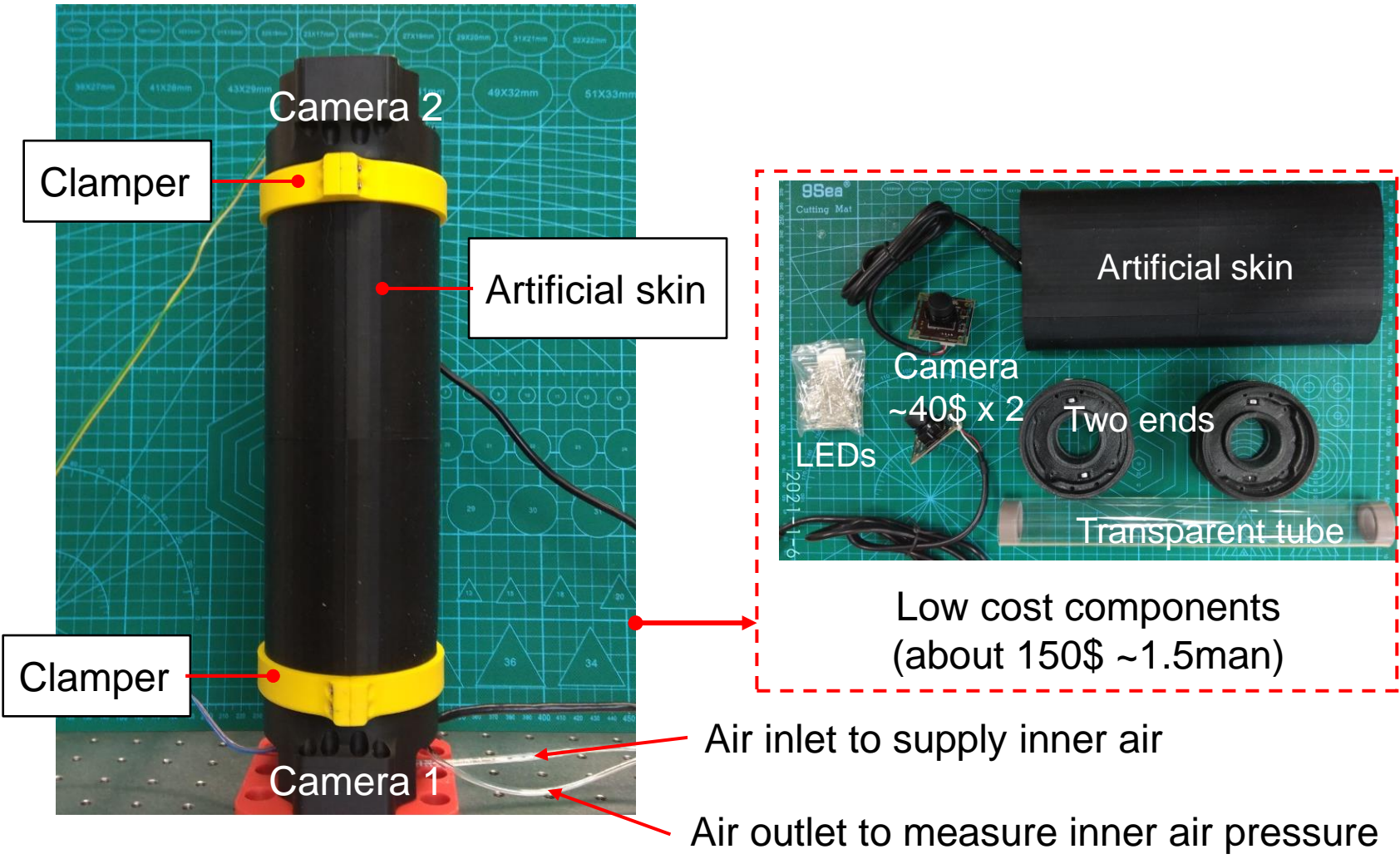
Top view



Step 3: Pouring silicone



Prototype model



2.4. Vision-Based Model

2.4.1. Mathematical Camera Model

2.4.2. Self-Calibration Technique

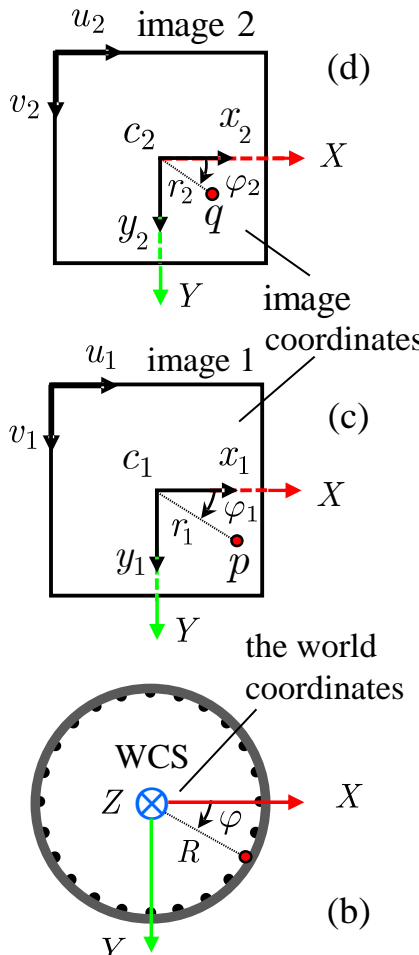
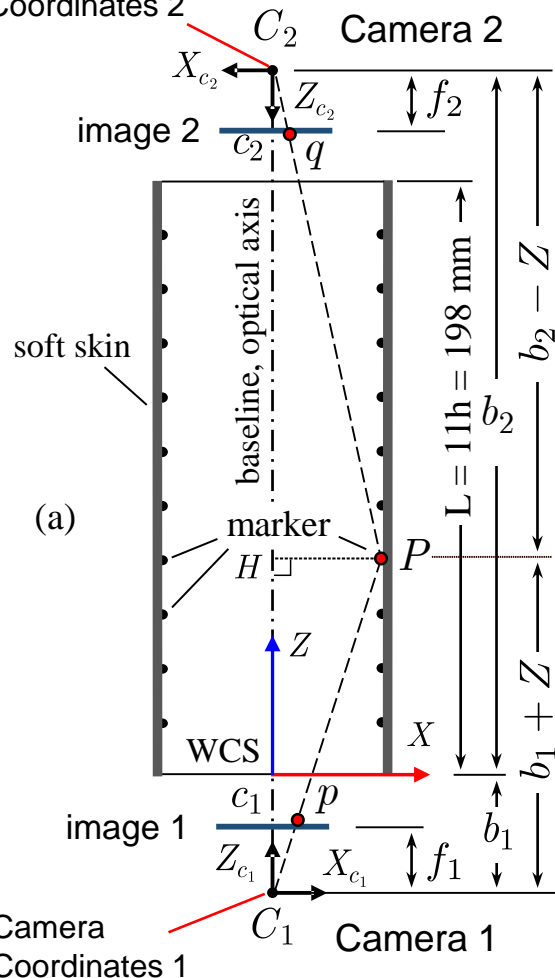
2.4.3. Stereo Registration

2.4.4. 3-D Reconstruction

2.4.5. Experimental Accuracy

2.4.1. Mathematical Camera Model

Camera
Coordinates 2



Noted:

- $P = (X, Y, Z)^T$ is a 3-D position of a marker
- $p = (x_1, y_1)^T$ and $q = (x_2, y_2)^T$ are the projections on two images
- $R = \sqrt{X^2 + Y^2}$, $r_1 = \sqrt{x_1^2 + y_1^2}$, $r_2 = \sqrt{x_2^2 + y_2^2}$ are radial coordinates
- $\varphi = \varphi_1 = \varphi_2$ is radial coordinates
- u_1, v_1 and u_2, v_2 are the two pixels coordinate systems
- $c_1(c_{x1}, c_{y1})$ and $c_2(c_{x2}, c_{y2})$ are two principal points
- WCS: World/Global Coordinate System

Determine $P = (X, Y, Z)$ from two projections $p = (x_1, y_1)$ and $q = (x_2, y_2)$

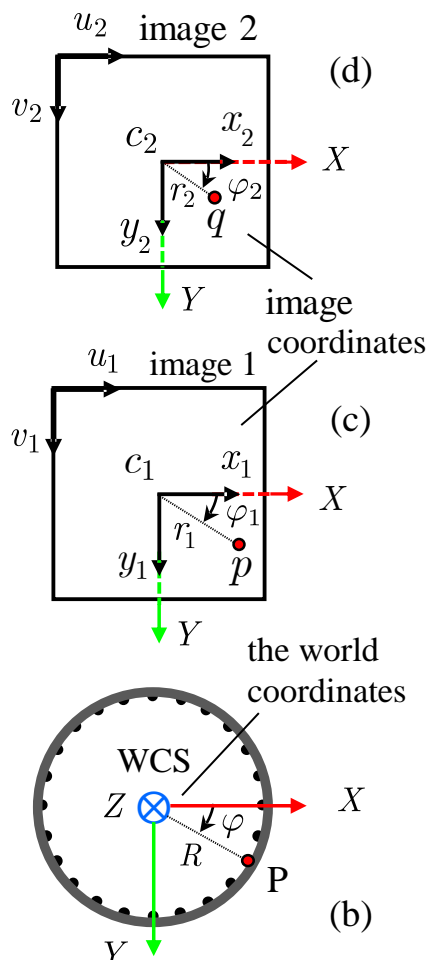
↳ (R, φ, Z) (cylindrical coord.)

↳ (r_1, φ_1)

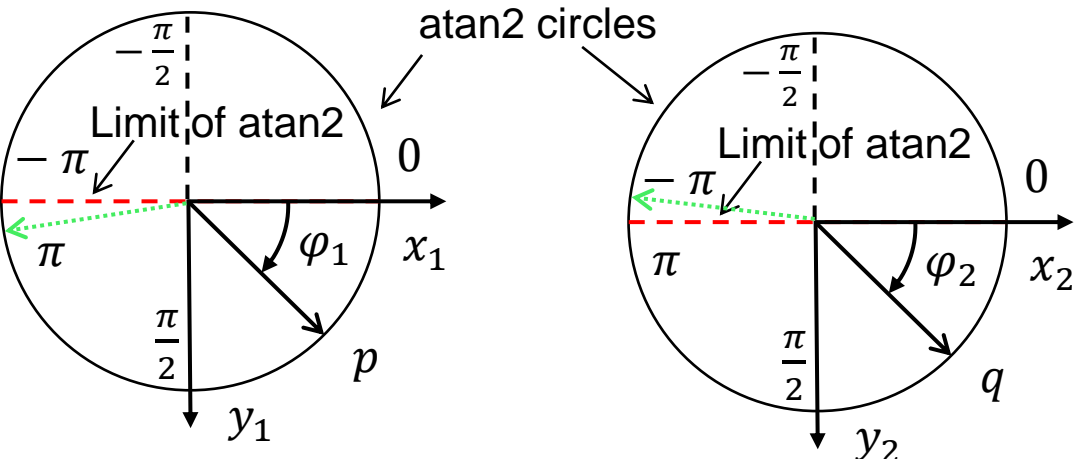
↳ (r_2, φ_2) (radial coord.)

2.4.1. Mathematical Camera Model

Because the cameras are installed symmetrically



$$\varphi = \varphi_1 = \varphi_2 \rightarrow \varphi = \frac{1}{2}(\varphi_1 + \varphi_2)$$



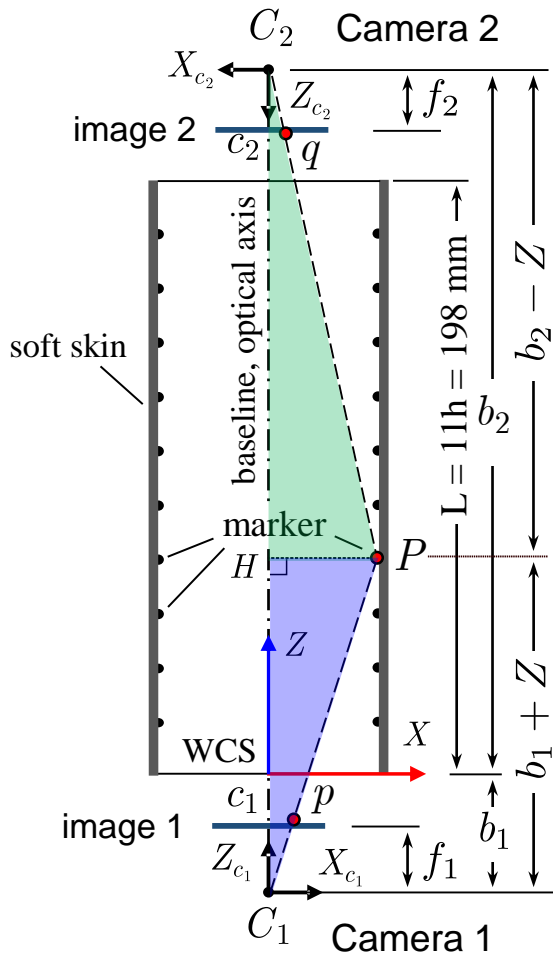
$$\varphi_1 = \text{atan2}(y_1, x_1)$$

$$\varphi_2 = \text{atan2}(y_2, x_2)$$

Since φ_1 and φ_2 discontinue at $-\pi$ and π , thus

$$\varphi = \begin{cases} 0.5(\varphi_1 + \varphi_2) & |\varphi_1 - \varphi_2| < \pi \\ 0.5(\varphi_1 + \varphi_2) - \pi \text{sign}(\varphi_1 + \varphi_2) & |\varphi_1 - \varphi_2| > \pi \end{cases}$$

2.4.1. Mathematical Camera Model



Camera Parameters:

$$\mathcal{C} = \{f_1, f_2, b_1, b_2\}$$

From $\Delta C_1 PH$ and $\Delta C_1 pc_1$ (camera 1):

$$p = \begin{bmatrix} x_1 \\ y_1 \end{bmatrix} = \frac{f_1}{b_1 + Z} \begin{bmatrix} X \\ Y \end{bmatrix} \rightarrow r_1 = \frac{f_1}{b_1 + Z} R$$

From $\Delta C_2 PH$ and $\Delta C_2 pc_2$ (camera 2):

$$q = \begin{bmatrix} x_2 \\ y_2 \end{bmatrix} = \frac{f_2}{b_2 - Z} \begin{bmatrix} X \\ Y \end{bmatrix} \rightarrow r_2 = \frac{f_2}{b_2 - Z} R$$

From above r_1 and r_2 relations, we have

$$Z = \frac{f_1 b_2 r_2 - f_2 b_1 r_1}{f_1 r_2 + f_2 r_1}$$

$$R = (b_1 + b_2) \frac{r_1 r_2}{f_1 r_2 + f_2 r_1}$$

$$\rightarrow X = R \cos(\varphi)$$

$$\rightarrow Y = R \sin(\varphi)$$

2.4.2. Self-Calibration Technique

The self-calibration strategy is based on the initial position of markers (240 markers) and their projections to determine the camera parameters

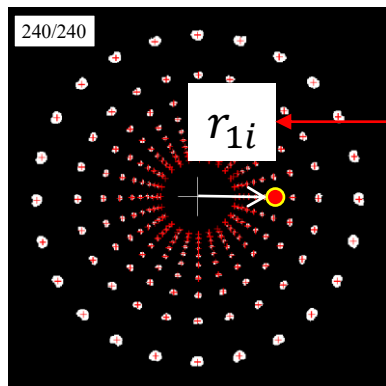


Image 2

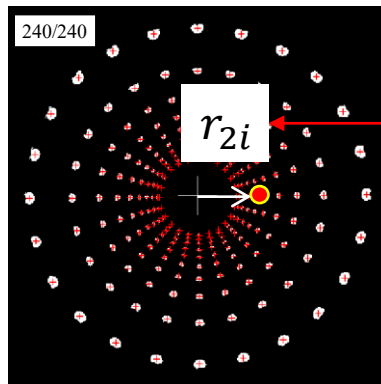


Image 1

Camera model



$$r_{1i} = \frac{f_1}{b_1 + Z_{0i}} R_{0i}$$

known

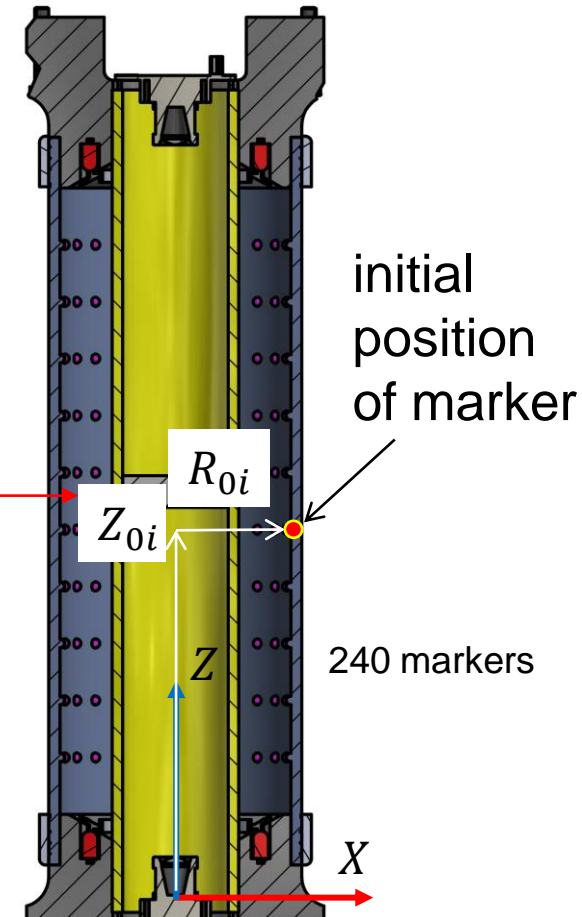
observed

$$r_{2i} = \frac{f_2}{b_2 - Z_{0i}} R_{0i}$$

known



$$\mathcal{C} = \{f_1, f_2, b_1, b_2\} = ?$$



Known 3-D initial position
 Z_{0i} and R_{0i}

Observed location r_{1i} and r_{2i}

2.4.2. Self-Calibration Technique

Step 1: Correct the lens distortion by radial division distortion model:

$$\text{undistorted} \rightarrow r_{1i} = \frac{\check{r}_{1i}}{1 + k_{11}\check{r}_{1i}^2 + k_{21}\check{r}_{1i}^4}, \quad r_{2i} = \frac{\check{r}_{2i}}{1 + k_{12}\check{r}_{2i}^2 + k_{22}\check{r}_{2i}^4}, i \in \mathcal{M}$$

Step 2: Approximate the parameters of cameras $\mathcal{C} = \{f_1, f_2, b_1, b_2\}$

$$\mathcal{C} = \arg \min_{\mathcal{C}} \left(\sum_{i \in \mathcal{M}} \|f_1 R_{0i} - r_{1i} b_1 - r_{1i} Z\|^2 + \|f_2 R_{0i} - r_{2i} b_1 - r_{2i} Z\|^2 \right)$$

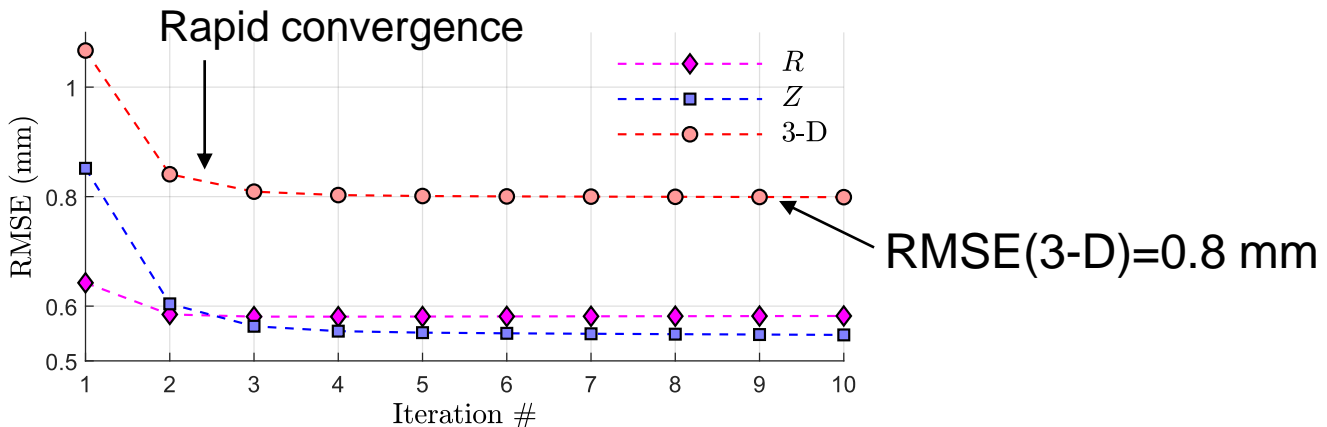
→ linear least-squares $\min_{\mathcal{C}} \|\mathbf{AC} - \mathbf{b}\|^2 \rightarrow \mathcal{C} = (\mathbf{A}^T \mathbf{A})^{-1} \mathbf{A}^T \mathbf{b}$

Step 3: Estimate the lens distortion coefficients $\mathcal{L} = \{k_{11}, k_{21}, k_{12}, k_{22}\}$

$$\mathcal{L} = \arg \min_{\mathcal{L}} \left(\sum_{i \in \mathcal{M}} \|r_{1i} \check{r}_{1i}^2 k_{11} + r_{1i} \check{r}_{1i}^4 k_{21} + (r_{1i} - \check{r}_{1i})\|^2 + \|r_{2i} \check{r}_{2i}^2 k_{11} + r_{2i} \check{r}_{2i}^4 k_{21} + (r_{2i} - \check{r}_{2i})\|^2 \right)$$

The calibration process loops these steps (i.e. 1 → 2 → 3 → 1 → ... → 3) until convergence to determine the cameras and lens parameters \mathcal{C} and \mathcal{L} .

2.4.2. Self-Calibration Technique



The RMSE (root mean square error) results for each iteration

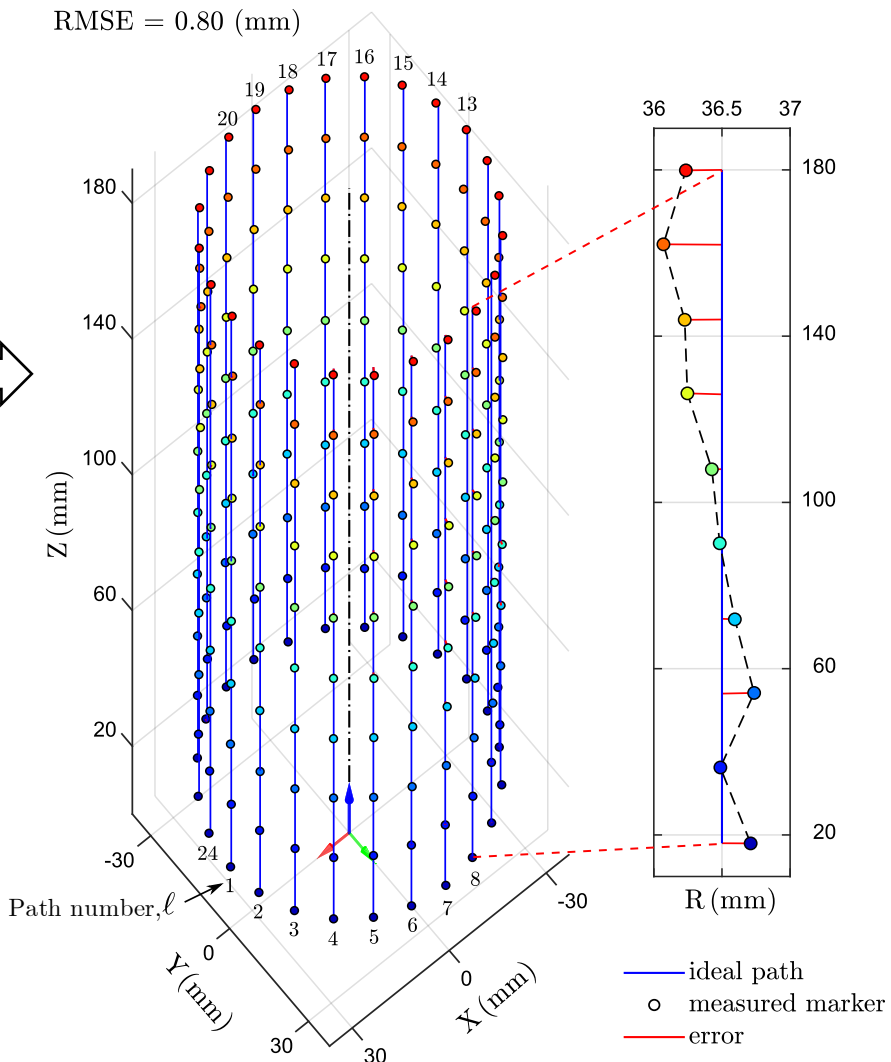
Parameters of cameras and lens distortion

Parameters	Camera 1	Camera 2	Units
f_i	226.91 ± 0.09	226.54 ± 0.06	pixels
b_i	26.50 ± 0.04	226.49 ± 0.02	mm
c_{x_i}	322.76 ± 0.01	299.70 ± 0.00	pixels
c_{y_i}	225.23 ± 0.01	251.89 ± 0.01	pixels
k_{1i}	27.85 ± 0.09	21.08 ± 0.10	$\times 10^{-7}$
k_{2i}	14.09 ± 0.04	11.58 ± 0.05	$\times 10^{-11}$

2.4.2. Self-Calibration Technique

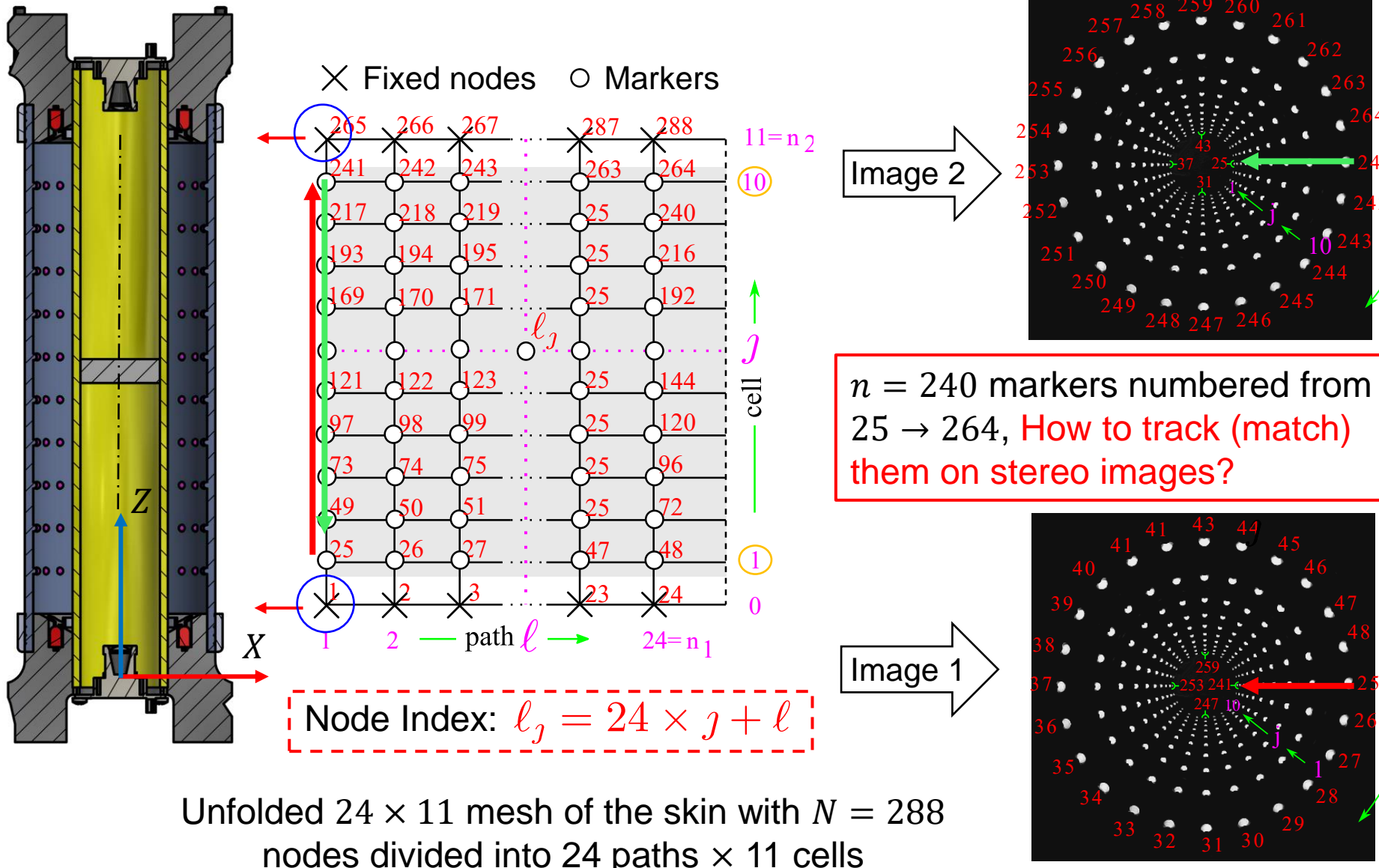
Camera model fits
the data well

$$D_{\text{marker}} = 2.8 \text{ mm}$$

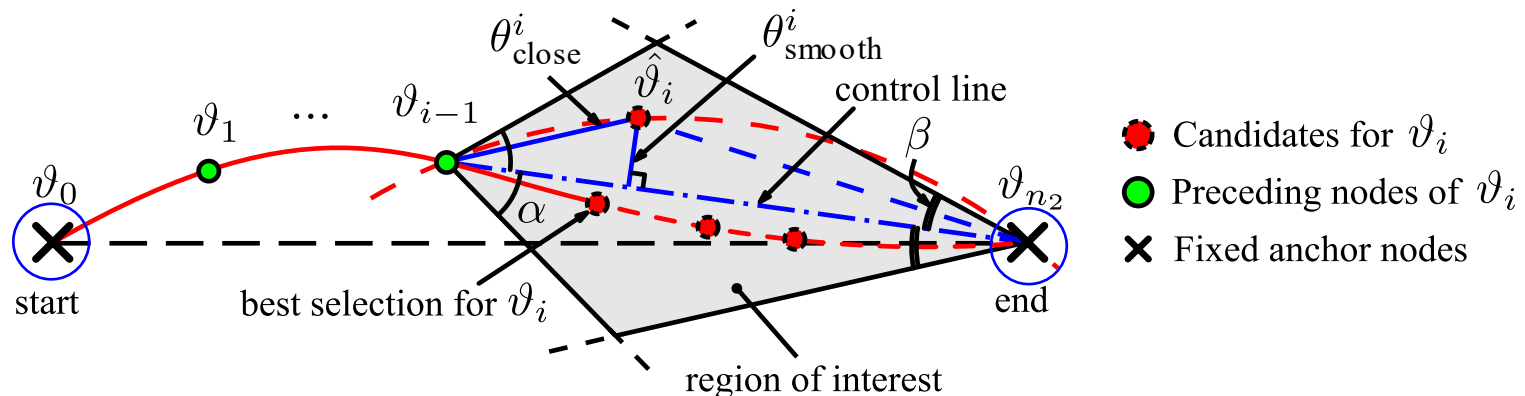


Recalculation of 3-D marker position using calibrated parameters

2.4.3. Stereo Registration



2.4.3. Stereo Registration



Given a set of marker points Φ , finding the unknown cells $\vartheta_i (i = 1 - 10)$ for a path with two fixed known points ϑ_0 and $\vartheta_{n_2} (n_2 = 11)$.

The proposed objective function combining closeness and smoothness terms to find a point ϑ_i is

$$\theta_{\text{obj}}^i(\hat{\vartheta}_i, \vartheta_{i-1}, \vartheta_{n_2}) = (1 - \lambda)\theta_{\text{close}}^i(\hat{\vartheta}_i, \vartheta_{i-1}) + \lambda\theta_{\text{smooth}}^i(\hat{\vartheta}_i, \vartheta_{i-1}, \vartheta_{n_2})$$

Then, ϑ_i is a point which minimizes the objective function as

$$\vartheta_i = \arg \min_{\hat{\vartheta}_i \in \Phi} \theta_{\text{obj}}^i(\hat{\vartheta}_i, \vartheta_{i-1}, \vartheta_{n_2})$$

Subject to: $\Delta \hat{\vartheta}_i \vartheta_{i-1} \vartheta_{n_2} < \alpha$ and $\Delta \hat{\vartheta}_i \vartheta_{n_2} \vartheta_{i-1} < \beta$

2.4.3. Stereo Registration

Image 1

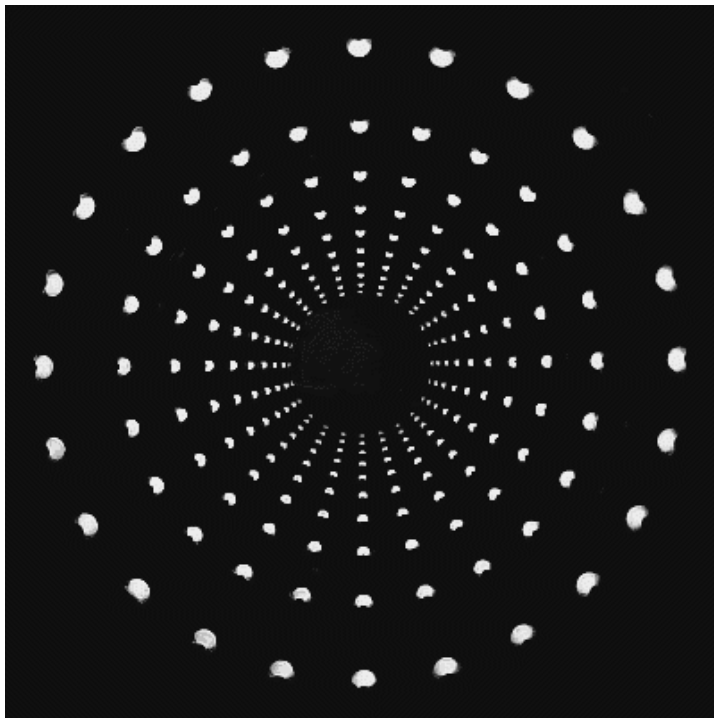
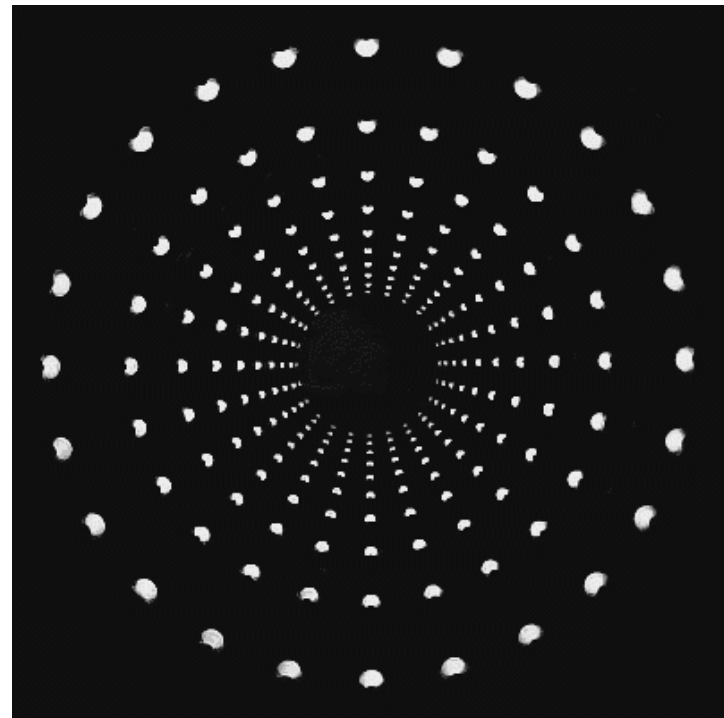


Image 2



$\Phi_1 \rightarrow I_1$ (organized)

$\Phi_2 \rightarrow I_2$ (organized)

After the registration algorithm, from detected sets of markers Φ_1 and Φ_2 , we obtain organized sets I_1 and I_2

2.4.4. 3-D Reconstruction

First, the marker P_{ℓ_j} (at path ℓ and cell j) is detected on two camera, the 3-D position is

$$P_{\ell_j} = \begin{bmatrix} X \\ Y \\ Z \end{bmatrix}_{\ell_j} = \begin{bmatrix} R\cos(\varphi) \\ R\sin(\varphi) \\ \frac{f_1 b_2 r_2 - f_2 b_1 r_1}{f_1 r_2 + f_2 r_1} \end{bmatrix}_{\ell_j}$$

Second, if the marker P_{ℓ_j} is detected only by one camera. The 3-D position is computed by either camera:

$$\begin{bmatrix} X \\ Y \end{bmatrix}_{\ell_j} = \frac{b_1 + Z_{\ell_j}}{f_1} \begin{bmatrix} x_1 \\ y_1 \end{bmatrix}_{\ell_j} \text{ or } \begin{bmatrix} X \\ Y \end{bmatrix}_{\ell_j} = \frac{b_2 - Z_{\ell_j}}{f_2} \begin{bmatrix} x_2 \\ y_2 \end{bmatrix}_{\ell_j}$$

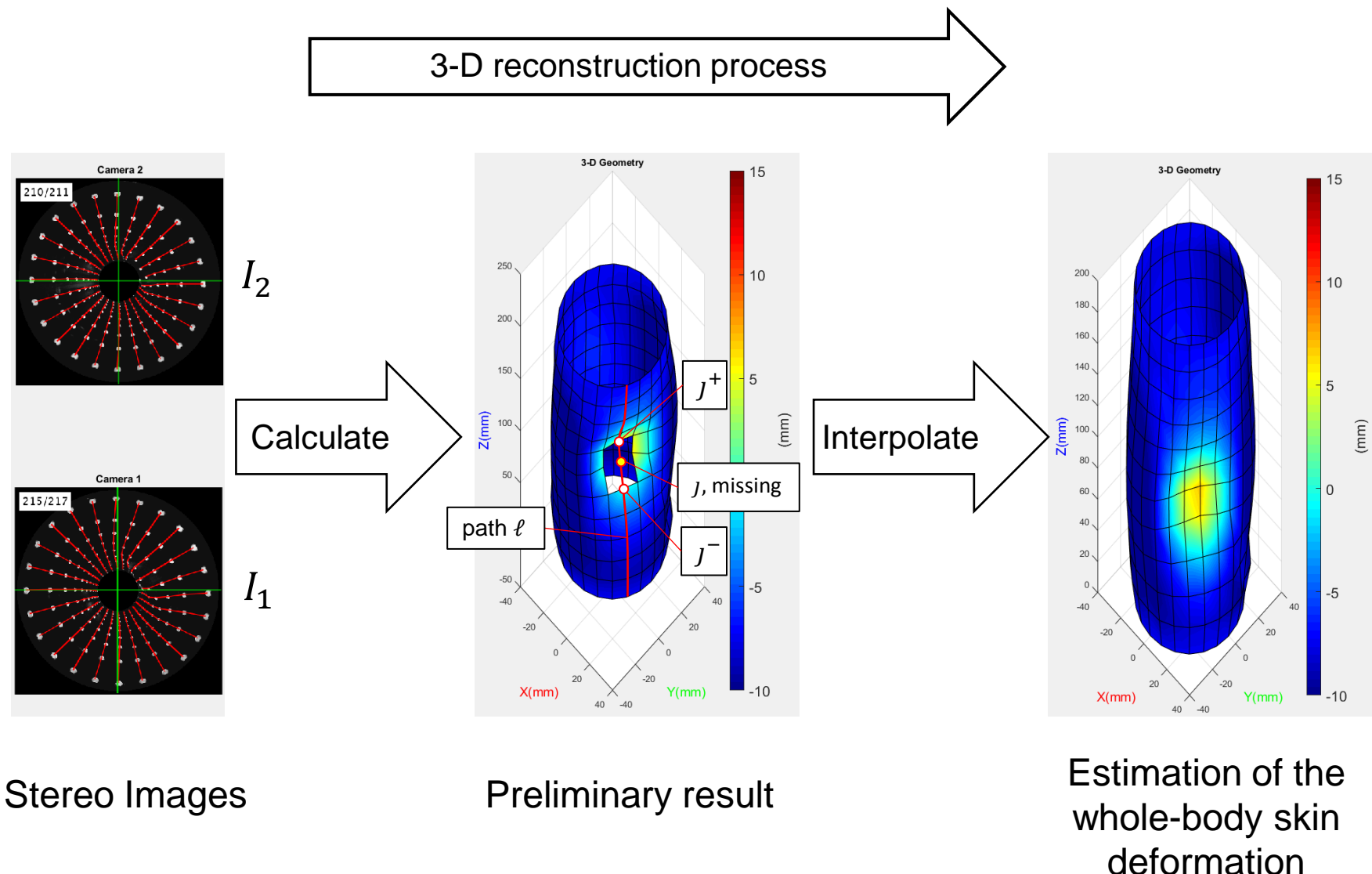
with $Z_{\ell_j} \approx jh$, as the initial position on the Z direction

Third, if the marker P_{ℓ_j} is missed on both cameras. The 3-D position is approximated by a linear interpolation at the same path:

$$P_{\ell_j} = w P_{\ell_{j^-}} + (1 - w) P_{\ell_{j^+}} \text{ with } w = \frac{j^+ - j}{j^+ - j^-}$$

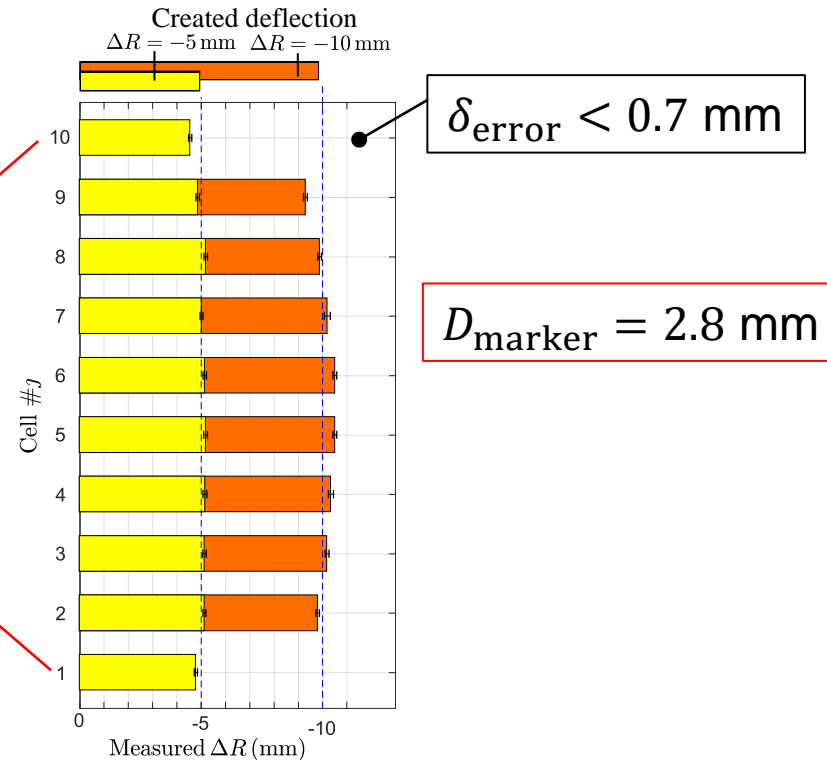
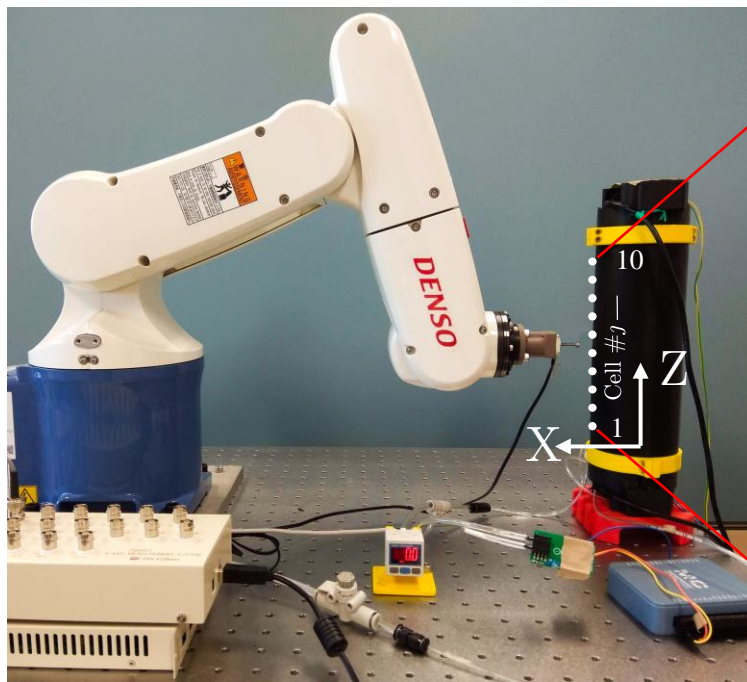
where j^- and j^+ are the two nearest nodes determined at path ℓ with $j^- < j < j^+$

2.4.4. 3-D Reconstruction



2.4.5. Experimental Accuracy

A robot arm pushes horizontally ($\Delta R = -5, -10 \text{ mm}$) at different nodes through a probe. The measured displacements are then compared with the robot motion.



The absolute error is lower than $0.7 \text{ mm} \triangleq \frac{0.7}{\text{FS}} = 5\% \text{FS}$ (full-scale = 15mm). However, this error may also derive from poor fabrication and installation with soft skin material.

2.5. Finite Element Model

2.5.1. Finite Element Method

2.5.2. Meshing the Skin

2.5.3. Shell Element Geometry

2.5.4. Element Equation

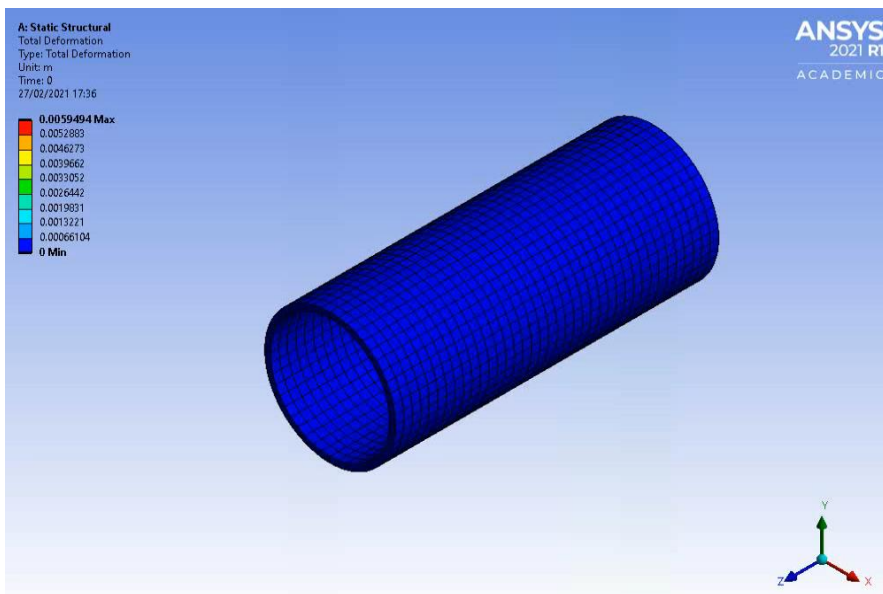
2.5.5. Global Equation

2.5.6. Finite Element Simulation

2.5.7. Young's Modulus Calibration

2.5.1. Finite Element Method

The finite element method (FEM) is a powerful method for mathematical modeling and solving engineering problems in various fields of mechanical analysis, heat transfer, electromagnetics, etc., in which a system is divided into a mesh of smaller elements.



Skin inflation simulation by ANSYS software:

- 12544 nodes
- 1824 elements

The commercial FEM softwares: ABAQUS, ANSYS, and COMSOL, etc. provide the pre-processing, solution, and post-processing functions, however, the core system of the FE model (FE equation) is not extractable.

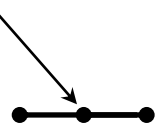
2.5.1. Finite Element Method

Types of finite elements

1-D

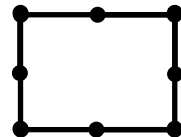
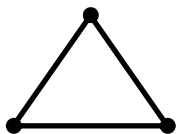


Mid-node

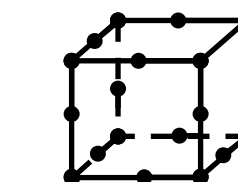
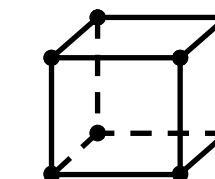
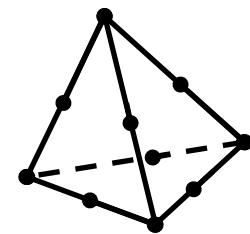
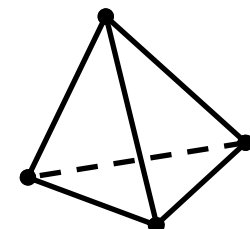


Beam, Truss

2-D



Plate, **Shell**



3-D

Order of interpolation



Linear
(1st)

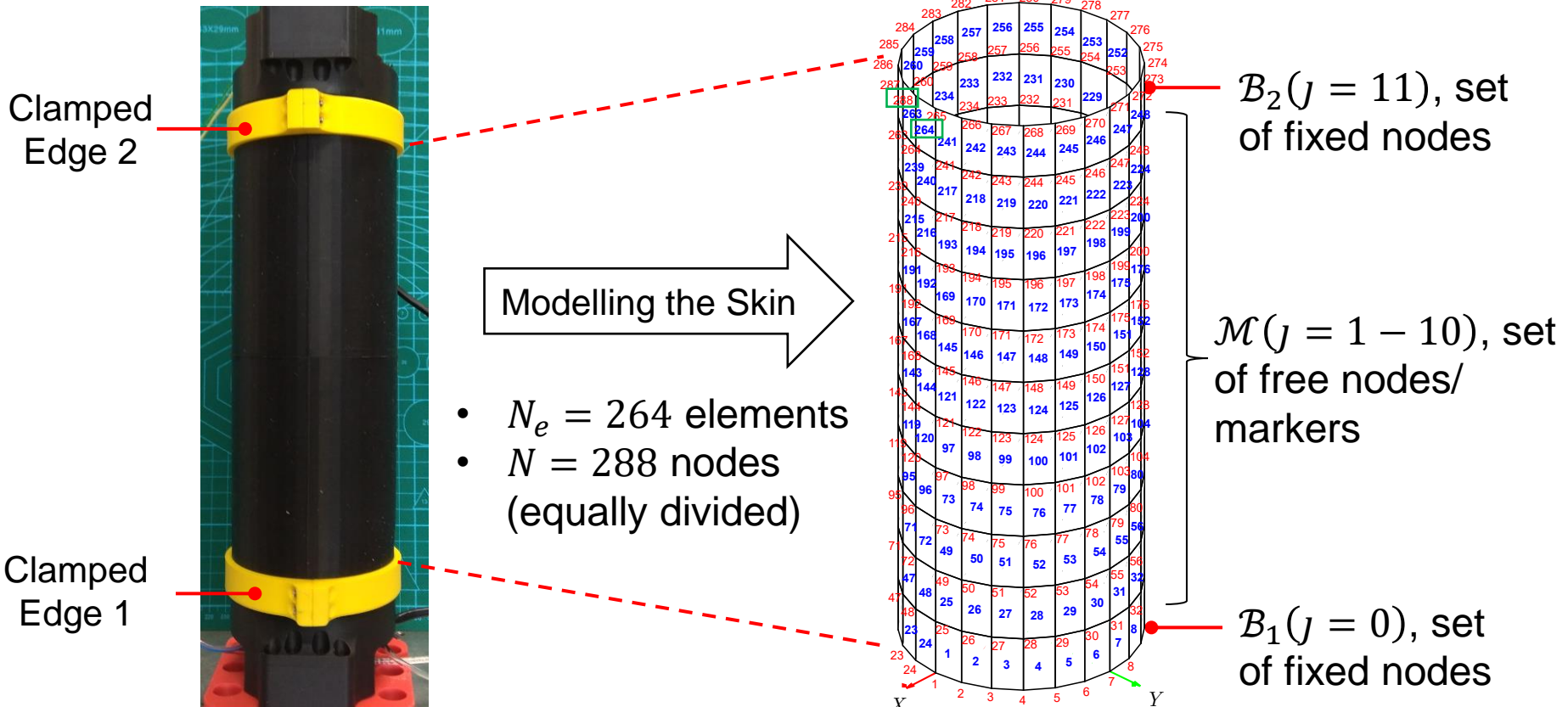
Quadratic
(2nd)

Solid

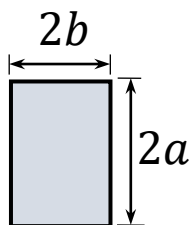
[Ch. 5, pp. 66-68]

- Since the skin is thin, i.e., $\frac{t}{R} = \frac{3.5}{36.5} < 10$. The shell element is selected.
- Higher-order of interpolation with mid-nodes (increase number/resolution of markers) can give a better representation of the geometry. *Trade-off between:*
Accuracy of FEM model vs Detectability of the Vision System

2.5.2. Meshing the Skin



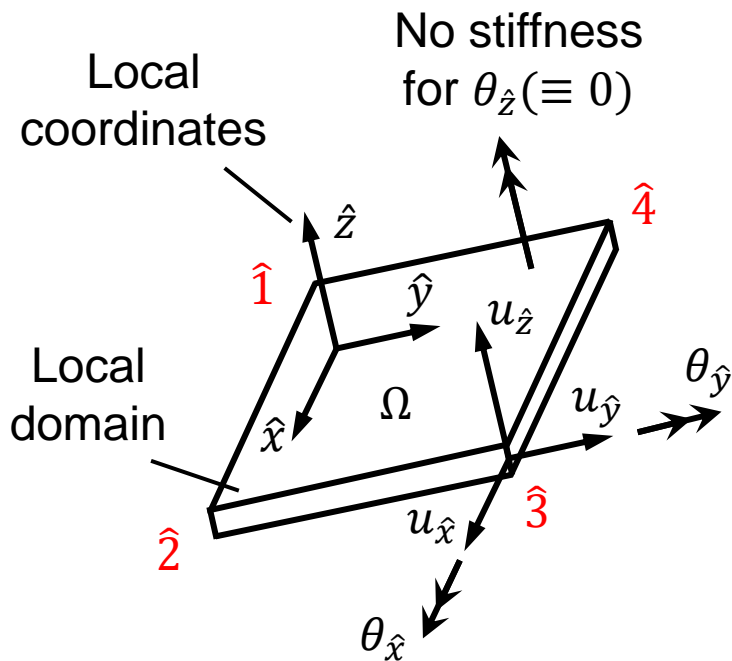
Real Artificial Skin



Finite Element Model

- $2a = h = 18 \text{ mm}$,
- $2b = 2R_0 \sin(\gamma/2) = 9.5 \text{ mm}$

2.5.3. Shell Element Geometry



Flat rectangular shell element
(thin thickness)

Five degrees of freedom (DOF) for every node of an element:

$$\mathbf{d}_{i(1-4)}^{(e)} = \begin{bmatrix} u_{\hat{x}_i} \\ u_{\hat{y}_i} \\ u_{\hat{z}_i} \\ \theta_{\hat{x}_i} \\ \theta_{\hat{y}_i} \end{bmatrix} \in \mathbb{R}^5, e = 1 - N_e$$

In-plane displacements

Bending displacements

Element displacement vector:

$$\mathbf{d}^{(e)} = \begin{bmatrix} \mathbf{d}_1^{(e)} \\ \mathbf{d}_2^{(e)} \\ \mathbf{d}_3^{(e)} \\ \mathbf{d}_4^{(e)} \end{bmatrix} \in \mathbb{R}^{20}, e = 1 - N_e$$

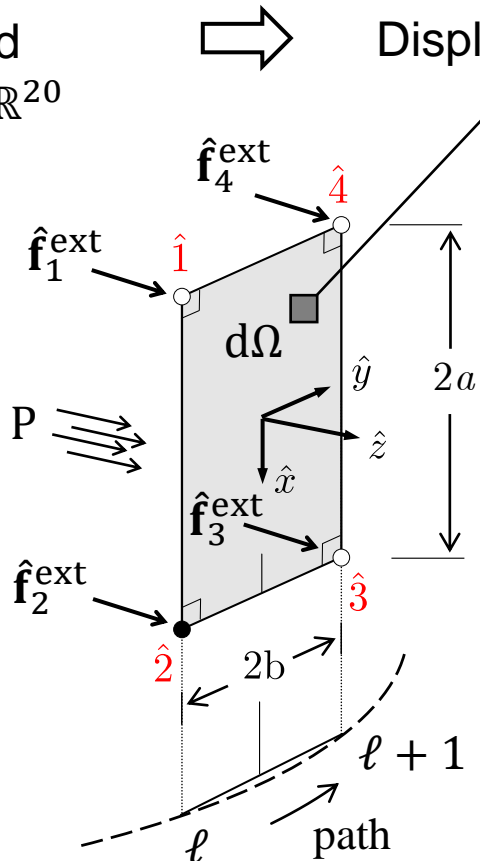
The total DOF of the system: $N \times 5 = 1440$ DOF, ($N = 288$ nodes)

2.5.4. Element Equation

Concentrated force $\hat{\mathbf{f}}^{\text{ext}} \in \mathbb{R}^{20}$

Surface load

$$\hat{\mathbf{s}} = \begin{bmatrix} 0 \\ 0 \\ P \\ 0 \\ 0 \end{bmatrix}$$



Static equilibrium of a shell element

$$\hat{\boldsymbol{\epsilon}} = [\epsilon_{\hat{x}}, \epsilon_{\hat{y}}, \gamma_{\hat{x}\hat{y}} \quad \kappa_{\hat{x}}, \kappa_{\hat{y}}, \kappa_{\hat{x}\hat{y}} \quad \gamma_{\hat{x}\hat{z}}, \gamma_{\hat{y}\hat{z}}]^T$$



Displacement $\hat{\mathbf{u}}$, strain $\hat{\boldsymbol{\epsilon}}$, and stress $\hat{\boldsymbol{\sigma}}$ fields

Principle of Virtual Work (PVW):

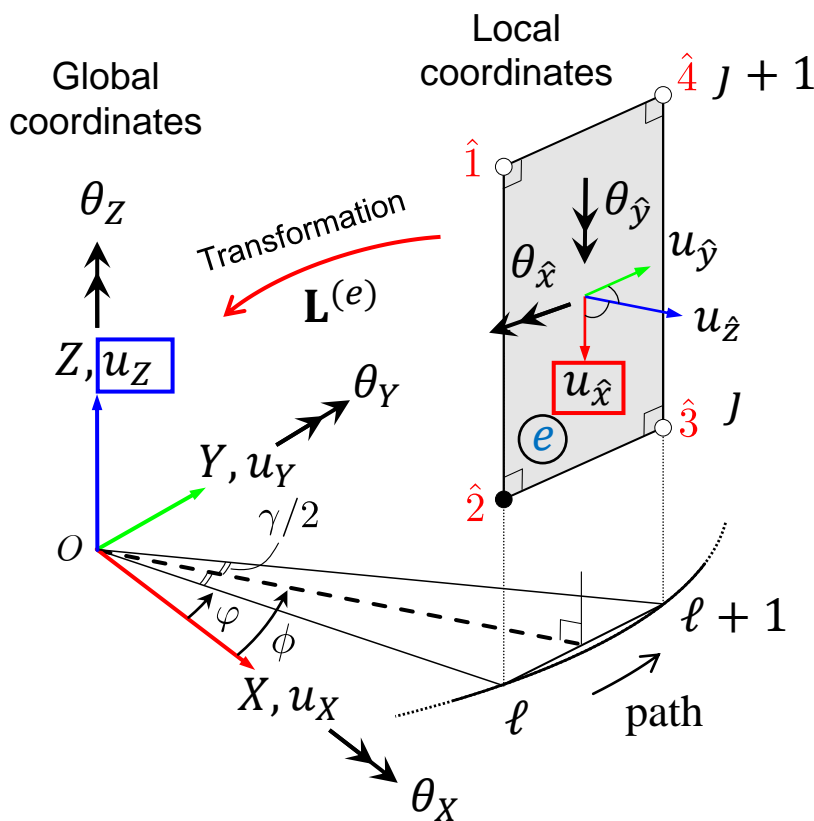
$$\int_{\Omega} \delta \hat{\mathbf{u}}^T \hat{\mathbf{s}} d\Omega + \delta \hat{\mathbf{d}}^T \hat{\mathbf{f}}^{\text{ext}} = \int_{\Omega} \delta \hat{\boldsymbol{\epsilon}}^T \hat{\boldsymbol{\sigma}} d\Omega$$

External virtual work Internal virtual strain energy

$$\Rightarrow \boxed{\hat{\mathbf{f}}_{\text{pressured}} + \hat{\mathbf{f}}^{\text{ext}} = \hat{\mathbf{k}} \hat{\mathbf{d}}}$$

- $\hat{\mathbf{u}} = \mathbf{N} \hat{\mathbf{d}}$ is the displacement field with $\mathbf{N}(\zeta, \eta)$ the shape matrix
- $\hat{\boldsymbol{\epsilon}} = \mathbf{B} \hat{\mathbf{d}}$ with \mathbf{B} the strain matrix
- $\hat{\boldsymbol{\sigma}} = \mathbf{C} \hat{\boldsymbol{\epsilon}} = \mathbf{C} \mathbf{B} \hat{\mathbf{d}}$ with \mathbf{C} the constitutive matrix of the material ($\mathbf{C} \propto E$, E is Young's modulus)
- $\hat{\mathbf{s}}$ is the surface load of the inner air pressure P

2.5.5. Global Equation



$$\phi = \varphi + \frac{\gamma}{2} = \left(\ell - \frac{1}{2}\right)\gamma$$

An element e at node (ℓ, J)
 $(\ell = 1 - 24, J = 0 - 11)$

$$\begin{bmatrix} u_{\hat{x}} \\ u_{\hat{y}} \\ u_{\hat{z}} \\ \theta_{\hat{x}} \\ \theta_y \end{bmatrix} = \underbrace{\begin{bmatrix} 0 & 0 & -1 & 0 & 0 & 0 \\ -s\phi & c\phi & 0 & 0 & 0 & 0 \\ c\phi & s\phi & 0 & 0 & 0 & 0 \\ 0 & 0 & 0 & s\phi & -c\phi & 0 \\ 0 & 0 & 0 & 0 & 0 & -1 \end{bmatrix}}_{\text{Local}} \underbrace{\mathbf{L}_{i(i=1-4)}^{(e)}(\phi)}_{\text{Element}} \begin{bmatrix} u_X \\ u_Y \\ u_Z \\ \theta_X \\ \theta_Y \\ \theta_Z \end{bmatrix}$$

The transformation matrix of an element e :

$$\mathbf{L}^{(e)} = \text{diagblock} \left(\mathbf{L}_1^{(e)}, \mathbf{L}_2^{(e)}, \mathbf{L}_3^{(e)}, \mathbf{L}_4^{(e)} \right)$$

$$\rightarrow \hat{\mathbf{d}}^{(e)} = \mathbf{L}^{(e)} \mathbf{d}^{(e)}, \mathbf{d}^{(e)} = \mathbf{L}^{(e)T} \hat{\mathbf{d}}^{(e)}$$

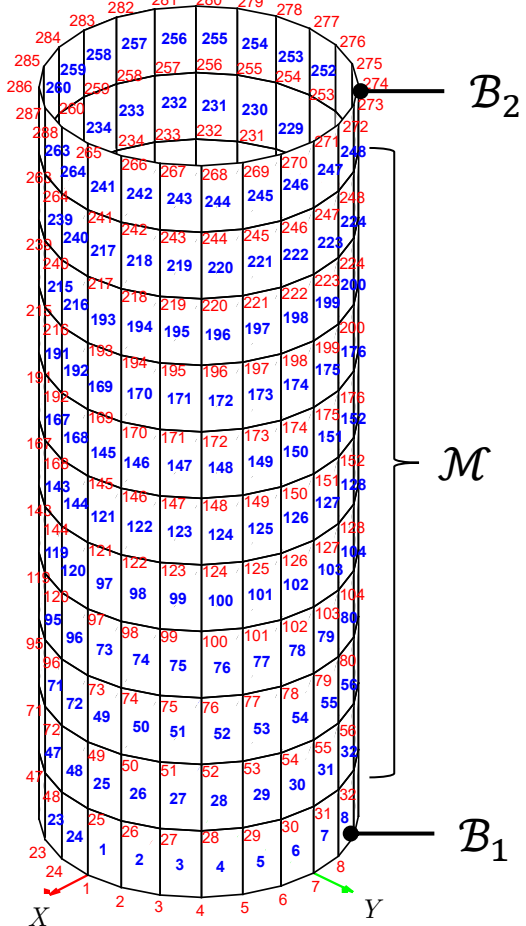
Element equation in the global coordinates

➡ $\mathbf{k}^{(e)} \mathbf{d}^{(e)} = \mathbf{f}_{\text{pressured}}^{(e)} + \mathbf{f}^{\text{ext}(e)}$

where

$$\mathbf{k}^{(e)} = \mathbf{L}^{(e)T} \hat{\mathbf{k}}^{(e)} \mathbf{L}^{(e)}; \mathbf{f}^{(e)} = \mathbf{L}^{(e)T} \hat{\mathbf{f}}^{(e)}$$

2.5.5. Global Equation



Mesh of $N_e = 264$ elements and
 $N = 288$ nodes
 $|\mathcal{B}_1| + |\mathcal{B}_2| + |\mathcal{M}| = 288$

Assembling all element equations $e = 1, 2, \dots, N_e$
 results in the global equation as

$$\mathbf{K}\mathbf{D} = \mathbf{F}_{\text{pressured}} + \mathbf{F}^{\text{ext}}$$

where $\mathbf{K} \in \mathbb{R}^{6N \times 6N}$ is the structural stiffness matrix,
 $\mathbf{D} \in \mathbb{R}^{6N}$ is the displacement vector.

The skin is clamped at two ends, thus the boundary condition of nodes on \mathcal{B}_1 and \mathcal{B}_2 is established as

$$\mathbf{D}_i = \mathbf{0}, i \in \mathcal{B}_1 \cup \mathcal{B}_2$$

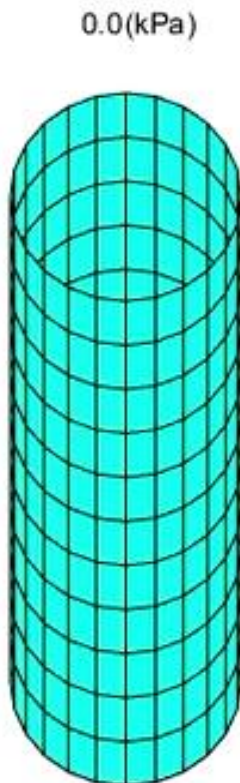
Mathematical relationship

$\mathbf{F}_{\text{pressured}}, \mathbf{F}^{\text{ext}}$
 (Force)

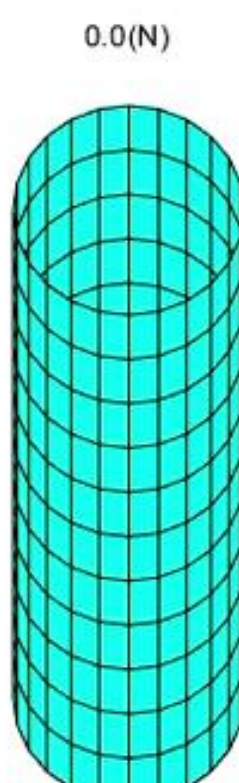
\mathbf{K}
 \longleftrightarrow
 \mathbf{D}
 (Displacement)

2.5.6. Finite Element Simulation

The response of the skin could be simulated in various contact scenarios



Inflation



Concentrated force



Generalized case

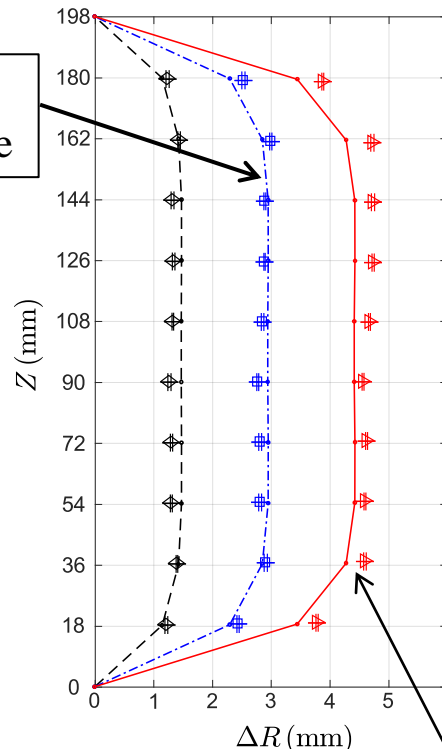
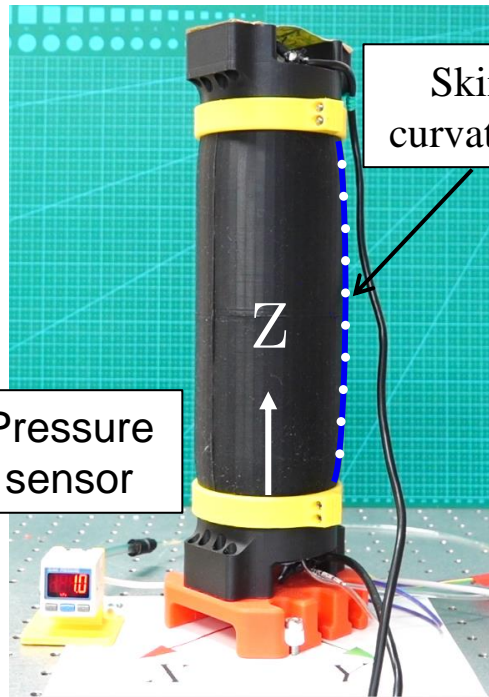
→ distributed force

→ concentrated force

→ reaction force

2.5.7. Young's Modulus Calibration

Young's modulus of the skin material (Ecoflex 50) was calibrated by a compression test at inner air pressures of 0.5kPa, 1kPa, and 1.5kPa.



Measured	FEM	
---	---	0.5 kPa
+	- - -	1.0 kPa
x	- - - -	1.5 kPa

Minimizing the difference:

$$\min_E \sum_P \left\| \mathbf{D}_{\text{measured}} - \frac{E^*}{E} \mathbf{D}_{\text{FEM}^*} \right\|^2$$

results in:

$$E = E^* \frac{\sum_P \|\mathbf{D}_{\text{FEM}^*}\|^2}{\sum_P \mathbf{D}_{\text{FEM}^*} \cdot \mathbf{D}_{\text{measured}}} \\ \approx 0.1 \text{ MPa}$$

(Noted: Reference FEM* model is assigned Young's modulus $E^* = 1 \text{ MPa}$)

$\text{RMSE}_{\text{calibrated}} = 0.38 \text{ mm}$
(root mean square error)

2.6. Tactile Force Reconstruction

2.6.1. Tactile Force Calculation

2.6.2. Sensitivity Evaluation

2.6.3. Experimental Evaluation

2.6.4. Demonstration Video

2.6.1. Tactile Force Calculation

Tactile force can be defined as the external force \mathbf{F}^{ext} acting on the skin body, excluding the distributed force $\mathbf{F}_{\text{pressured}}$ generated by inner air pressure:

$$\mathbf{F}^{\text{tac}} \triangleq \mathbf{F}^{\text{ext}} = \mathbf{K}\mathbf{D}_{\text{measured}} - \mathbf{F}_{\text{pressured}}$$

with the displacement vector \mathbf{D} is provided from the vision system as:

$$\mathbf{D}_{\text{measured},i} = \begin{bmatrix} u_{X_i} \\ u_{Y_i} \\ u_{Z_i} \\ \theta_{X_i} \\ \theta_{Y_i} \\ \theta_{Z_i} \end{bmatrix} \triangleq \begin{bmatrix} u_{X_i} \\ u_{Y_i} \\ u_{Z_i} \\ 0 \\ 0 \\ 0 \end{bmatrix} = \begin{bmatrix} X_i - X_{0i} \\ Y_i - Y_{0i} \\ Z_i - Z_{0i} \\ 0 \\ 0 \\ 0 \end{bmatrix}, \quad i = 1, 2, \dots, N, (N = 288)$$

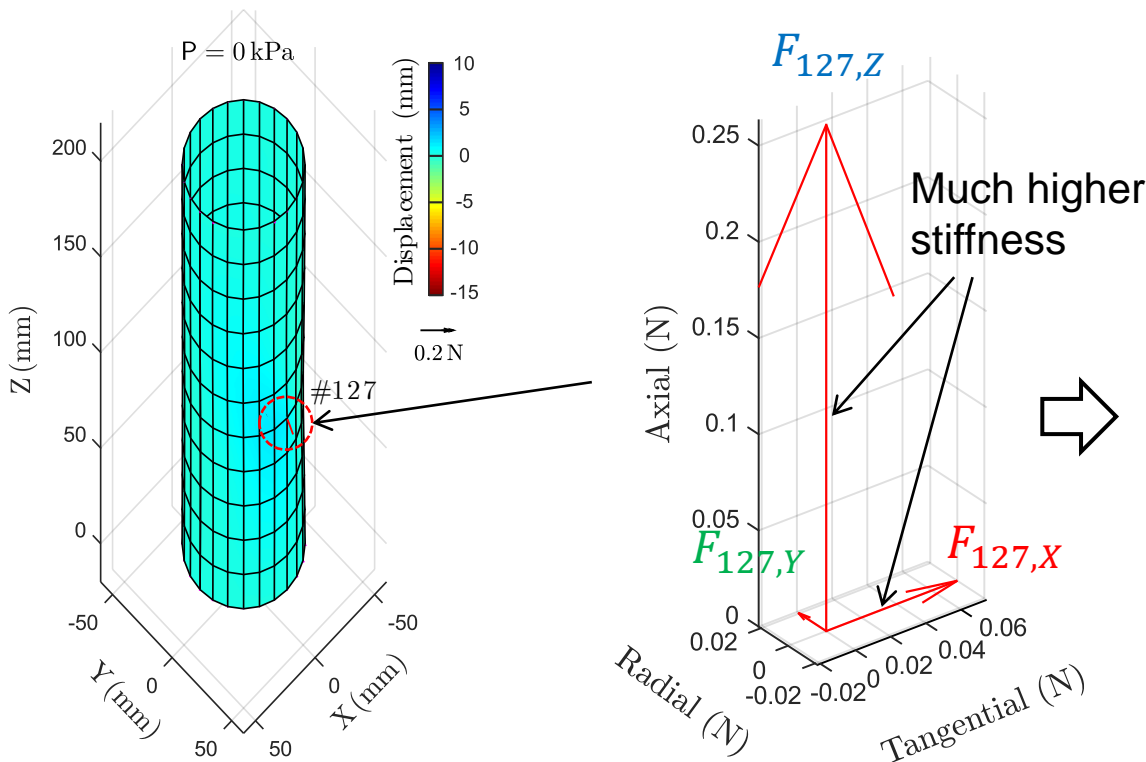
↑
Displacement of node i

└→ Ignoring rotation degrees of freedom

where (X_i, Y_i, Z_i) and (X_{0i}, Y_{0i}, Z_{0i}) are the measured and initial 3-D position of node i , respectively.

2.6.2. Sensitivity Evaluation

To evaluate the sensitivity on the **tangential**, **radial**, and **axial** directions. Lets constrain note #127 as $\mathbf{D}_{127} = [\delta \ \delta \ \delta \ 0 \ 0 \ 0]^T$, δ (mm) is assumed the position measurement error in each direction.



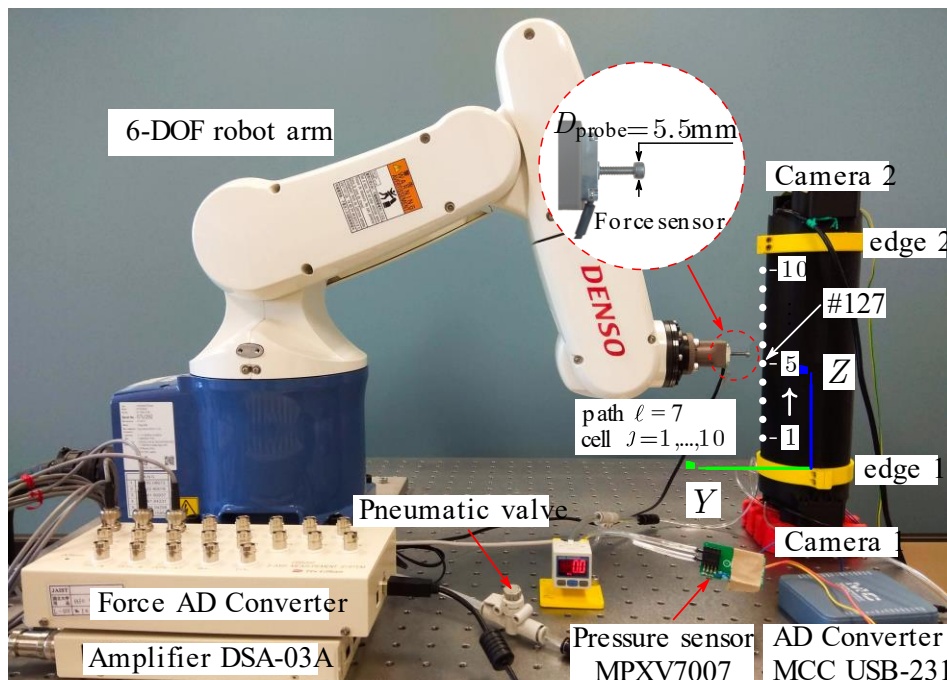
resulting in reaction force at node #127 as:

$$\mathbf{F}_{127}^{\text{ext}} = \begin{bmatrix} F_{127,X} \\ F_{127,Y} \\ F_{127,Z} \\ M_{127,X} \\ M_{127,Y} \\ M_{127,Z} \end{bmatrix} = \begin{bmatrix} 0.08\delta(N) \\ 0.02\delta(N) \\ 0.30\delta(N) \\ 0 \\ 0 \\ 0 \end{bmatrix}$$

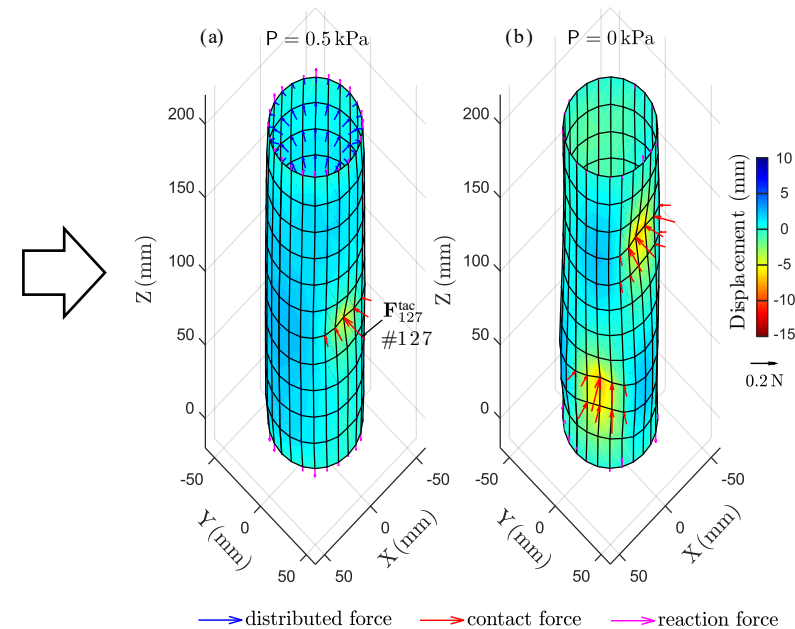
The error of the tactile force is much higher in the tangential (~4 times) and axial (~15 times) than radial direction. Thus, to ensure reliability, only radial force component ($f_R = F_X \cos \varphi + F_Y \sin \varphi$), higher a certain threshold $f_{\text{thresh}} = 0.02\delta(N)$, is considered.

2.6.3. Experimental Evaluation

To evaluate the single point contact, a robot arm attached a force sensor on its end-effector pushes horizontally ($\Delta R = -5, -10 \text{ mm}$) at nodes #127 via a probe in different inner air pressure conditions (0, 0.5, 1, 1.5) kPa. The probing force (force sensor) is then compared with tactile force of TacLINK (F_{127}^{tac}) and FE simulation (F_{127}^{ext}) at note #127.

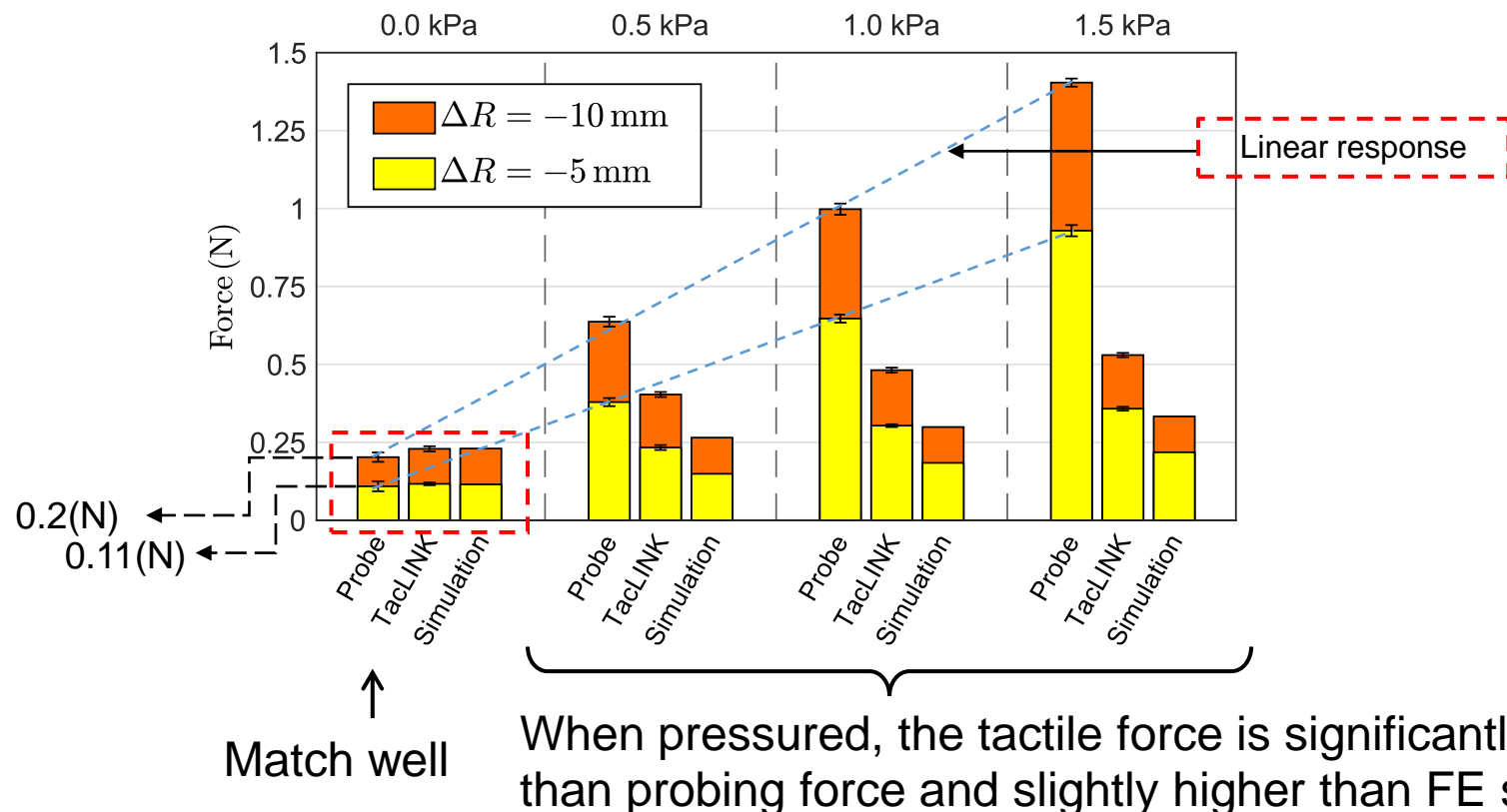


Experiment setup



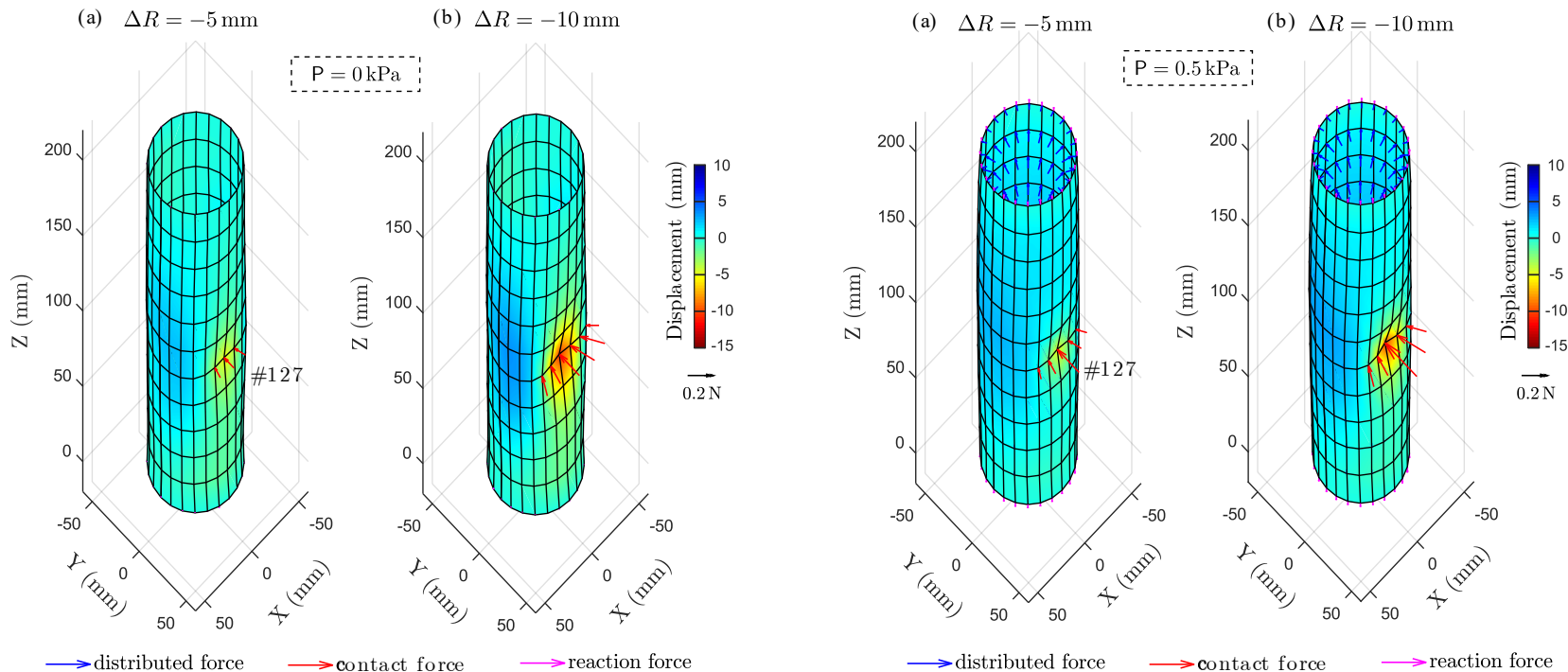
Whole-body tactile force perceived by TacLINK

2.6.3. Experimental Evaluation



- The resultant forces are linear in terms of displacement and inner air pressure
- It is challenge to create an ideal point load by a probe and perceive by a nodal tactile force. Because of the finite size of the probe ($D_{probe} = 5.5 \text{ mm} \gg 0$) and non-ideal model of the prototype.

2.6.3. Experimental Evaluation



Whole-body tactile force sensing performance

- The tactile force is also distributed on the neighbor nodes (since the probe has a finite area $S_{\text{contact}} \triangleq S_{\text{probe}} = \pi \frac{D_{\text{probe}}^2}{4} \sim 23.8 \text{ mm}^2 \gg 0$).
- But the largest force is at the contacted node #127. Thus, TacLINK is capable in sensing tactile force distribution.

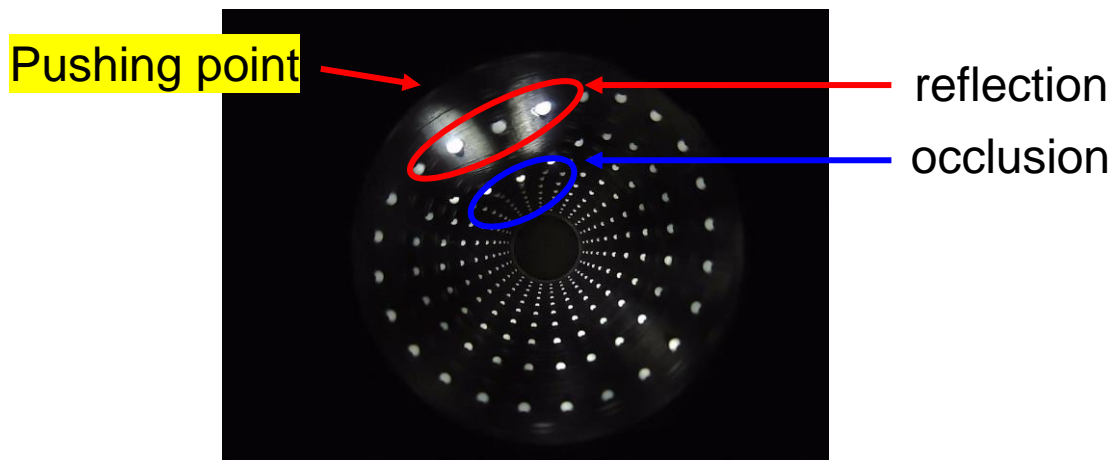
2.6.4. Demonstration Video



III. Discussion

1. The Proposed Vision-Based Tactile Force Sensing: [Ch. 7, pp. 107-108]

- The vision system is significantly affected by reflection and occlusion, resulting in the proposed 3-D reconstruction may not represent well the actual position of markers. The researches in the design and fabrication of the skin to reduce occlusion and light reflection are needed to efficiently utilize on the other systems.



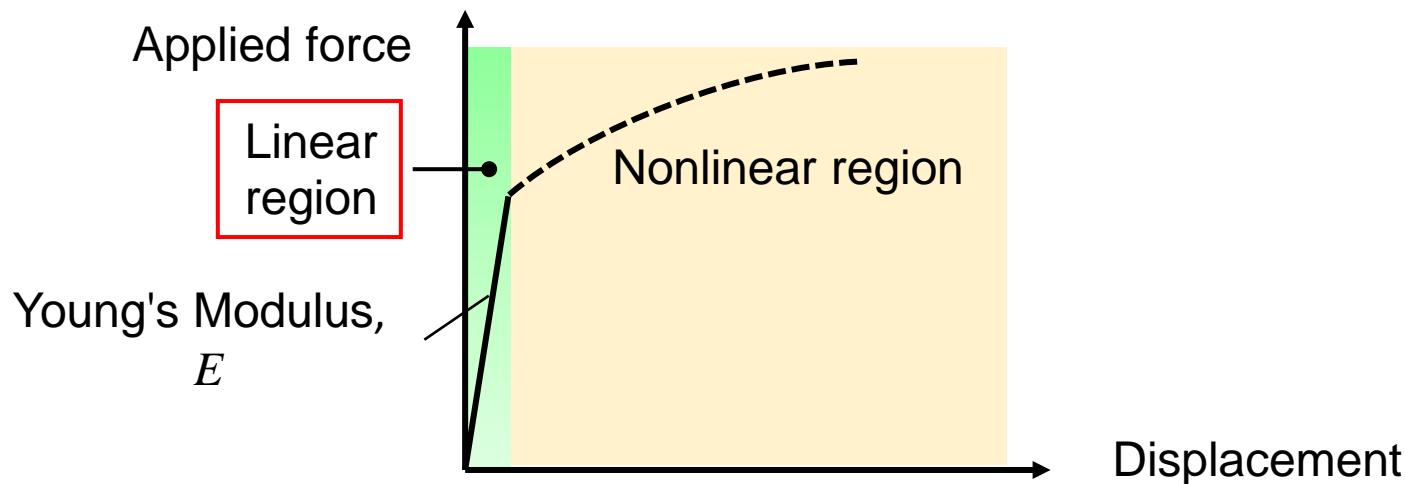
- The speed of TacLINK is now ~15Hz (with camera frame rate ~30 FPS) which should be more improved with a higher camera specification and a high-speed processing system (e.g., FPGA) to enhance the speed of a sensing system.

III. Discussion

2. FE Model and Material Nonlinearity:

[Ch. 5, pp. 108-109]

- The proposed linear FE model requires linear elastic material and small deformation (linear region), i.e., stiffness matrix remains constant. This phenomenon may not suitably describe the non-linear region. Thus, further investigations of material characteristics are needed to describe the response of the skin accurately.



- The proposed FEM is only suitable to the skin with shell structure, so to utilize the proposed sensing technique to more general shapes, the more complex formulations of FEM (e.g., solid elements) are also needed.

IV. Conclusion

Using only two cameras on a simple structure, the proposed system using the finite element method can efficiently construct the distribution of forces acting on the whole-body surface of TacLINK.

The contributions of the research could be summarized as below

- 1) A *novel large-scale tactile sensing system at low-cost for robot links*:** TacLINK is designed for robot links with a large sensing area of about 500cm² but low cost (~150\$) and high performance in sensing both contact geometry and contact force.
- 2) An *efficient vision-based tactile sensing system*:** The proposed vision system including two facing cameras with proposed algorithms tracks efficiently displacements of all the markers locating on the inner wall of the hollow elongated cylinder skin surface. This vision system can be utilized for other similar systems, such as prosthetic arms, legs, etc.

IV. Conclusion

3) The finite element method (FEM) for tactile force sensing: This research utilized the FEM to derive the stiffness matrix of the skin that is a key to calculate the contact force of the vision-based tactile sensors. Besides, we could evaluate, optimize the design for a specified application based on the FE model.

4) A highly scalable structure and a generalized technique to develop the vision-based tactile sensing devices: The proposed artificial skin with markers is very simple, customizable, and easily fabricated by the casting method. The analytical FEM provides the structural stiffness of the skin. The vision system can be designed by a set of cameras to track the displacements of the skin. Thus, the research expects to contribute a generalized method for designing vision-based tactile devices.

V. Future Work and Outlook

The future works of the research are:

- 1) The future will continue to investigate and solve the mentioned issues (e.g., light reflection, sensing speed, optimization, material nonlinearity).
- 2) Utilize the proposed design technique on other parts of robots, such as fingers, arms, chests, legs, foots, and prosthetics for humans, etc.
- 3) Develop the tactile-based interactive controls for robotics to enable safe and intelligent interactions with humans.

The outlooks for future research and development are:

- 1) *New generations of the robot with whole-body tactile sensing:* The robot could safely and intelligently interact and manipulate through the sense of touch.
- 2) *Human-like prosthetics with tactile sensation:* The generation of prosthetics with artificial sensing and nerve is very promising in practice. Future smart prosthetics could help the handicapped person perceiving pain, sense real-world objects, etc.

Publication

Journal Papers:

1. **L. Van Duong** and V. A. Ho, "Large-Scale Vision-Based Tactile Sensing for Robot Links: Design, Modeling, and Evaluation," in *IEEE Transactions on Robotics (T-RO)**^{*}, vol. 37, no. 2, pp. 390-403, April 2021, doi: 10.1109/TRO.2020.3031251. (reviewed by eight reviewers)

**: Eigenfactor: 0.01428 (#1 in robotics), total citations: 14,259 (#1 in robotics), impact factor: 6.123 (#2 in robotics).*

International Conference Papers:

1. **L. Van Duong**, R. Asahina, J. Wang, and V. A. Ho, "Development of a Vision-Based Soft Tactile Muscularis," 2019 2nd IEEE International Conference on Soft Robotics (RoboSoft), Seoul, Korea (South), 2019, pp. 343-348, doi: 10.1109/ROBOSOFT.2019.8722814.

Patent:

1. ホ アンヴァン, **Duong**, 朝比奈, 触覚検知装置及び触覚検知方法, 出願番号: 2019-018391 (2019/02/05)

Reference

- [1] L. E. Osborn *et al.*, "Prosthesis with neuromorphic multilayered e-dermis perceives touch and pain." *Sci. Robot.*, 3, eaat3818, 2018.
- [2] J. Reinecke *et al.*, "Experimental comparison of slip detection strategies by tactile sensing with the BioTac on the DLR hand arm system," *2014 IEEE Int. Conf. Robot. and Autom. (ICRA)*, Hong Kong, 2014, pp.2742-2748.
- [3] Sun Q *et al.*, "Active Matrix Electronic Skin Strain Sensor Based on Piezopotential Powered Graphene Transistors," *Adv Mater.*, 2015, Art. no 27(22):3411-7
- [4] Wang S. *et al.*, "Skin electronics from scalable fabrication of an intrinsically stretchable transistor array," *Nature*, 2018, Art. no. 555, 83-88.
- [5] B. Li *et al.*, "Mechanical Imaging of Soft Tissues With a Highly Compliant Tactile Sensing Array," in *IEEE Trans. on Biomedical Engineering*, vol. 65, no. 3, pp. 687-697, March 2018.
- [6] A. Schmitz *et al.*, "Methods and technologies for the implementation of large-scale robot tactile sensors," *IEEE Trans. Robot.*, vol. 27, no. 3, pp. 389–400, Jun. 2011.
- [7] G. Cheng *et al.*, "A comprehensive realization of robot skin: Sensors, sensing, control, and applications," *Proc. IEEE*, vol. 107, no. 10, pp. 2034-2051, 2019
- [8] W. Yuan *et al.*, "GelSight: High-resolution robot tactile sensors for estimating geometry and force," *Sensors*, vol. 17, no. 12, 2017, Art. no. 2762.
- [9] Sato, K., Kamiyama, K., Kawakami, N., Tachi, and S., "Finger-shaped GelForce: Sensor for measuring surface traction fields for robotic hand," *IEEE Trans. Haptics*, vol. 3, no. 1, pp. 37–47, Jan.–Mar. 2010.
- [10] B. Ward-Cherrier *et al.*, "The TacTip family: Soft optical tactile sensors with 3D-Printed biomimetic morphologies," *Soft Robot.*, vol. 5, no. 2, pp. 216–227, 2018.
- [11] E. Onate, "Structural analysis with the finite element method linear statics, in: Beams, Plates and Shells of Lecture Notes on Numerical Methods in Engineering and Sciences," vol. 2, Springer, Berlin, 2013.
- [12] Y. W. Kwon *et al.*, "The Finite Element Method Using MATLAB. Boca Raton," FL, USA, CRC Press, Inc., 2000.

Acknowledgment

I would like to deeply thank the MEXT* scholarship for financially supporting my Ph.D. period at JAIST from Oct. 2018 to Sep. 2021.

Thanks HO sensei, thesis committee, professors, and all members of JAIST for helping and supporting my study.

(*) MEXT Program 2018 by School of Materials Science, JAIST: Global Energy-Environment-Health Innovation Program (GEEHIP).



Any
Questions

Thank you

